Magnetic properties of layered nanostructures studied by means of Brillouin light scattering

and the surface magneto-optical Kerr effect

Magnetic properties of layered nanostructures studied by means of Brillouin light scattering and the surface magneto-optical Kerr effect

Giovanni Carlotti and Gianluca Gubbiotti

INFM and Dipartimento di Fisica dell'Università, Via Pascoli, 06123 Perugia, Italy

Abstract
Brillouin light scattering (BLS) and the surface magneto-optical Kerr effect (SMOKE) provide two well established, non-destructive, optical techniques whose combined use can yield a great deal of information about magnetism in low-dimensional systems, such as thin films, multilayers, and patterned structures. The former technique gives information on the high-frequency dynamical properties of a spin system, through detection of long-wavelength spin waves, while the latter permits easy and direct access to the orientation of the magnetization and to its evolution with the applied magnetic field. Both techniques can be implemented *in situ*, to study thin magnetic films and nanostructures in ultrahigh-vacuum conditions. In this article the main characteristics of both BLS and the SMOKE are discussed and a few experiments carried out at GHOST laboratory, Perugia University, are presented, with emphasis given to the complementarity of the two techniques.

(Some figures in this article are in colour only in the electronic version)

1. Introduction

The enormous interest in magnetism in thin films and nanostructures demands new techniques able to yield deep insight into the magnetic properties of such systems. In this paper, the main characteristics and a few applications of Brillouin light scattering (BLS) [1–4] and the surface magneto-optical Kerr effect (SMOKE) [5, 6] will be reviewed. The former gives information on the high-frequency dynamical properties of a spin system, while the latter permits easy and direct access to the magnetization orientation and to its evolution with the applied magnetic field.

The study of dynamical magnetic excitations in ultrathin films and superlattices has to face the problem that the inelastic neutron scattering technique, usually exploited in the case of bulk materials, is not sensitive enough because of the reduced interaction volume. This gulf of information has been partially filled in the past using ferromagnetic resonance (FMR) [7],

which is based on the microwave absorption by a system with precessing spin. However, FMR is restricted to spin excitations with zero wavevector which are uniform across the specimen and do not exhibit dipolar coupling in layered structures. In addition, in an FMR experiment one measures the average magnetic properties of a millimetre-size specimen and investigation is generally limited to a single frequency. These limitations have been overcome using the BLS technique which relies upon the inelastic scattering of photons by thermally activated spin waves. During the last decade, the BLS technique has proved to be very effective for detecting spin waves in ultrathin films and multilayered structures, with a sensitivity down to the monolayer scale. In a BLS experiment, a beam of highly monochromatic light is focused on the surface of the magnetic film under investigation and the light scattered within a solid angle is frequency analysed using a multi-pass Fabry–Perot interferometer (FPI). Because of the wavevector conservation in the magnon–photon interaction, the wavelength of the revealed spin waves is of the same order of magnitude of that of light. This means that the wavelength of the spin waves revealed in a BLS experiment, even if shorter than in FMR experiments, is much larger than the interatomic distances, so the material can be described as a continuum within an effective-medium approach. From BLS measurements of the spin-wave frequencies as a function of the direction and magnitude of the in-plane wavevector, $q_\parallel$, and of the direction and strength of the externally applied magnetic field, a determination of magnetic parameters, such as gyromagnetic ratio, saturation magnetization, anisotropy constants, and exchange constants, can be achieved. In the case of multilayered structures, composed of either alternating magnetic/non-magnetic or magnetic/magnetic layers [8], the BLS technique provides access to the interlayer exchange constant, too. Another important characteristic of the BLS technique is that it is a non-destructive local technique (the probed area of the sample is of the order of $10 \times 10 \ \mu$m) and this permits one to perform a scan of the magnetic properties of inhomogeneous specimens, such as wedge-shaped films and multilayers. In addition to ultrathin films consisting of a few atomic layers, the BLS technique can be successfully applied to the study of rather thick single films and multilayers. In fact, in spite of the small penetration depth of light in metallic media (about 10 nm), the information gained by the BLS technique concerns the whole coherence depth of the spin waves, which is of the order of a few hundreds of nanometres.

Reflection of a beam of linearly polarized light from a magnetized surface causes the polarization to become elliptical, with the principal axis rotated with respect to the incoming light. Usually the amount of rotation (in radians) and of ellipticity (the ratio between the minor and major axes of the ellipse) induced in the reflected beam are of the order of 10^{-3}–10^{-4}, i.e. relatively small. This phenomenon is known as the magneto-optical Kerr effect (MOKE). In the case of ultrathin films with total thickness below about 10 nm, the effect is proportional to the film thickness and the name becomes the 'SMOKE'. The SMOKE technique is mainly used to measure the hysteresis loops of thin magnetic films, by plotting the signal (rotation or ellipticity) as a function of the applied magnetic field. Unfortunately, such a signal is proportional to the magnetization, and an absolute quantitative estimation of it requires the use of other magnetometry techniques, such as vibrating-sample magnetometry (VSM). The MOKE can also be used as the basis of a scanning microscopy technique, so magnetic domain imaging with micrometric resolution becomes possible [9]. Even submicrometric resolution can be achieved by combining magneto-optical measurements with a scanning near-field optical microscopy (SNOM) apparatus. Unfortunately, such a combination can be currently exploited only for a few materials and experimental work remains to be done to permit routine operation in reflection (rather than in transmission) [10].

The SMOKE and BLS techniques have been extensively used in the last decade for studying magnetization behaviour and magnetic anisotropy in ultrathin epitaxial films. They

permitted the magnetic order in ultrathin films consisting of a few atomic layers to be investigated. This problem is of very great interest, since it is known from the Mermin and Wagner theorem [11] that magnetic order cannot exist in a two-dimensional isotropic Heisenberg ferromagnet. In spite of this, it has been shown that magnetic anisotropies can lead to stable two-dimensional ferromagnetic ordering and that dipolar interactions play an important role in this process [12]. Important progress in the study of magnetic films as thin as a few monolayers has recently been achieved through *in situ* SMOKE and BLS technique operation within the ultrahigh-vacuum (UHV) chamber where the films were grown. This allows a complete study of magnetic films directly in UHV conditions, avoiding any contamination and the need for a protective overlayer. This innovation opens the way to the study of a number of interesting issues, such as the dependence of interface anisotropy on both the temperature and the presence of a specific non-magnetic overlayer [13], which have received little attention to date and still need thorough experimental investigation.

The structure of this paper is as follows. Sections 2 and 3 are aimed at giving a combined presentation of the physical and experimental principles of the BLS and SMOKE techniques. In section 4 the theoretical approach which can be used to calculate the spin-wave frequency in thin films is outlined. Section 5 presents a review of selected experiments mainly carried out at GHOST (group of high-resolution optical spectroscopy and related techniques) Laboratory, Perugia University [14]. Emphasis is given to the importance of a combined BLS and SMOKE study, showing the complementarity of the two techniques. Finally, section 6 presents the conclusions.

2. The Brillouin scattering technique

It is well known that collective excitations in a solid can inelastically scatter incident light, through the induced modulation of the optical constants of the medium. In analogy with the elasto-optic effect caused by acoustic phonons, in the case of spin waves this is achieved via the magneto-optic interaction. This can be understood as the fluctuation of the transverse polarizability of a medium due to the Lorentz force caused by the precessing magnetization. In the magnetic case, however, the scattering tensor is always off-diagonal because the polarizability is perpendicular to both the electric field of the incoming light and to the fluctuating magnetization. The polarization of the scattered light is therefore perpendicular to that of the incident light. In addition, if one considers the transverse nature of electromagnetic waves, it turns out that in the geometries where the fluctuating magnetization can only generate a polarizability parallel to the light propagation direction it remains, to first-order approximation, ineffective. This happens, for instance, when the wavevector of the incoming light, and the static magnetization, M, are collinear. Therefore, one usually chooses geometries where the wavevector of incoming light is perpendicular to the magnetization direction.

Providing an alternative approach to that based on the modulation of the optical constant of the medium, BLS can be understood in very simple terms either as a Doppler shift of the frequency of light scattered from a propagating spin wave or as a photon–magnon collision in which the frequency and the momentum are conserved.

In a typical Brillouin scattering experiment one measures spin waves with frequencies in the range between about 1 and 150 GHz. In order to extract the weak inelastic component of light from the elastically scattered contribution, a high-resolution spectrometer is required. To this end, the best combination of high resolution and good throughput is achieved using a FPI [15] as a scanning spectrometer. In opaque materials, it is usual for the intensity of the elastically scattered light to exceed that of the Brillouin component by more than a factor of 10^4–10^5, so the contrast of a single interferometer is not sufficient for making measurements
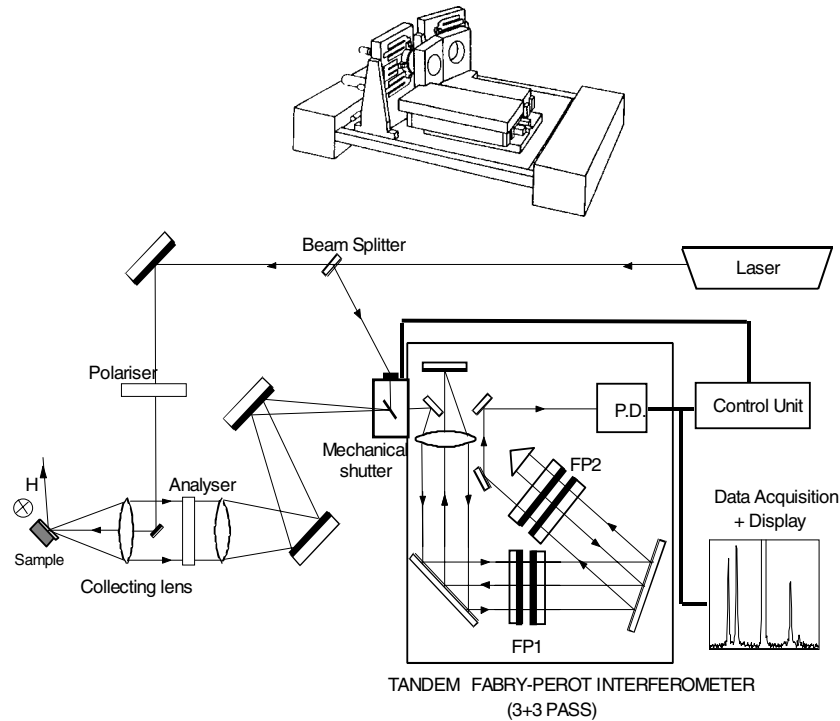
Figure 1. Upper part: a diagram of the actual tandem interferometer mounted on two dynamical antivibration mounts. Lower part: a diagram of the whole Brillouin scattering apparatus.

in such a situation. A way to increase the spectral contrast is to introduce multi-pass operation: by sending the light back through the same interferometer a few times, the contrast can be increased to values close to 10^{10} and this is sufficient for Brillouin scattering experiments on opaque materials.

In order to avoid the overlap of neighbouring interference orders and extend the range of frequency investigated, it is possible to combine two interferometers of unequal mirror spacing (tandem operation). In the Sandercock interferometer this condition is achieved by mounting the interferometers on the same scanning stage, one with the mirror axis parallel to the scan direction and the other offset by an angle of about 20°. A detailed description of this instrument can be found in [16] and [17].

Figure 1 shows schematic representations of the real interferometer stage and the whole experimental apparatus used for BLS experiments in the backscattering configuration, which is usually exploited in experiments on thin films and layered structures. In addition to the box containing the tandem–multipass interferometer and the optical components necessary for the multipass operation (3 + 3 passes in our case), one can see the external optics which is needed to focus the incident laser beam onto the surface of the specimen. In a typical experiment the specimen is placed between the poles of an electromagnet with the external magnetic field applied perpendicular to the scattering plane and parallel to the film surface. In backscattering geometry the same lens (usually a commercial camera objective) is used to focus light and to collect the backscattered photons for analysis through the interferometers. In this geometry, due to the conservation of the wavevector component parallel to the film

surface, the wavevector of magnons revealed in the spectra is linked to the optical wavevector k_I by the simple relation

$$q_\parallel = 2k_I \sin \theta_i \tag{1}$$

where θ_i is the angle of incidence of light. In order to reduce the noise level and to suppress signals from acoustic phonons, an analyser is placed at the entrance of the interferometer in order to stop scattered photons whose polarization is parallel to that of incident photons.

3. The SMOKE technique

As stated above, the Kerr effect consists in the change of the polarization state of a beam of light when reflected by the surface of an opaque magnetized medium. It is the analogue of the well known Faraday effect, which occurs in the case of transmission through a transparent medium. To a first approximation, if the incident beam is linearly polarized, the degrees of rotation and of ellipticity affecting the reflected beam are proportional to the magnetization of the medium. In addition, in the case of film thickness below about 10 nm, the signal is also proportional to the film thickness and one usually calls this the SMOKE technique, where 'S' stands for 'surface'.

Although a microscopic explanation of magneto-optical effects would have to consider the coupling between the electrical field of the polarized light and the electron spin within the magnetic medium which occurs through the spin–orbit interaction, a simple interpretation is usually achieved from a macroscopic point of view, where magneto-optical effects arise from the antisymmetric, off-diagonal elements in the dielectric tensor. In particular, the magneto-optical effect can be understood on the basis of different responses of the electrons to left- and right-polarized electromagnetic waves. In fact, a linearly polarized beam of light can be thought of as a superposition of two such waves. Electrons will be driven into left circular motion by the left-polarized wave while the right-polarized wave will drive them into right circular motion, with equal radii of the orbits. Now, since the dipole moment is proportional to this radius, an external magnetic field applied in the propagation direction will cause an additional Lorentz force to act on each electron. As a consequence, the radius for the left circular motion will be reduced and the radius for the right circular motion will be increased, with the result that the emerging light is elliptically (instead of linearly) polarized.

Experimentally, there are three principal configuration geometries in operation of the MOKE technique, as shown in figure 2. In the longitudinal configuration the magnetic field is applied parallel to both the plane of the film and the plane of incidence of the light. The measured signal (either rotation or ellipticity) is proportional to the component of the magnetization contained in the plane of incidence of the light. This configuration is very useful when one wants to measure the hysteresis cycle of a film characterized by an in-plane magnetization. Polar geometry, instead, is exploited to gain information on the component of the magnetization that is perpendicular to the film plane. The magnetic field is applied perpendicular to the plane of the film. The experimental set-up normally involves passing laser light through a polarizer and then reflecting the light off the sample. The light then passes through another cross-polarizing analyser. Slight changes in the plane of polarization will thus cause variations in the detected light intensity after the second filter [5]. Modulation of the laser source or of the light polarization, in combination with lock-in amplification of the detected signal, helps to increase the signal-to-noise ratio. Use of an additional quarter-wavelength plate permits one to measure the Kerr ellipticity. As a more effective alternative to the crossed-polarizers method, a differential method using a Wollaston prism and two identical detectors can also be exploited, as shown in figure 3. Again, either the rotation
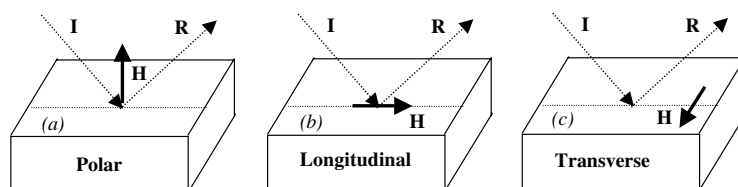
Figure 2. Schematic depictions of the polar, longitudinal, and transverse Kerr effect geometries. The Kerr effect in each particular geometry is sensitive to the magnetization changes along the directions indicated by the orientation of the externally applied field H. Dotted arrows indicate the direction of the incident ('I') and of the reflected ('R') light beam.
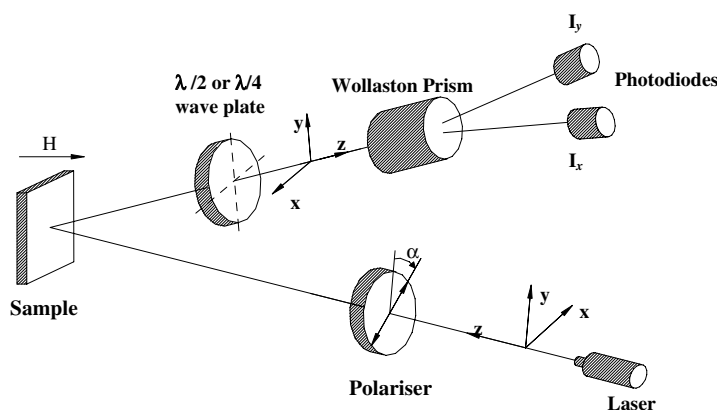

Figure 3. A schematic diagram of the SMOKE apparatus used in the differential method. The acquired signal is $\frac{I_x - I_y}{I_x + I_y}$. It is proportional to either the Kerr rotation or ellipticity, depending on the retardation plate used.

or the ellipticity of the reflected light can be measured, depending on the use of either a half-wavelength or a quarter-wavelength retardation plate. Finally, in the transverse MOKE technique the magnetic field is applied perpendicular to the plane of incidence of the light. This geometry provides a signal proportional to the component of magnetization that is parallel to the film plane but perpendicular to the plane of incidence of the light. In this case there is no polarization modification of the reflected light, but a change in the intensity of linearly polarized incident light is detected.

A recent development related to the MOKE is so-called quantitative vector magnetometry (MOKE–VM) [18], which permits one to quantitatively evaluate the different magnetization components, including the modulus of the magnetization vector. This method, which relies upon measurements of the MOKE signal in at least three different configurations of the light polarization and of the applied field, yields an accurate and complete characterization that enables a three-dimensional tracking down of the magnetization vector while the external field is swept along certain directions. In this way one can go beyond a qualitative description of the switching process, obtaining a deeper insight into the mechanism of magnetization reversal within the hysteresis loop for materials displaying anisotropy (both crystalline and shape originated), revealing to what extent magnetization reversal occurs via coherent magnetization rotation and allowing for the identification of the easy and hard axes [19]. This is relevant, especially in the case of magnetic domain formation, where the modulus of the magnetization vector exhibits a marked decrease.

Finally, the recent interest in laterally finite microstructures has pushed several groups into exploiting the MOKE in a microscopy technique. The magneto-optical signal is recorded while a focused laser beam is scanned over the sample surface, achieving micrometric resolution. This technique can therefore be used to derive evidence of magnetic domain structures.

4. Long-wavelength spin waves in layered systems: a general approach

4.1. Spin waves in the dipolar–exchange regime

Even if exchange interaction is responsible for the magnetic ordering, magnetic dipole–dipole interaction is also present in a system of spins. This latter interaction is typically very much smaller than the exchange interaction between neighbouring sites (often by two or three orders of magnitude), and therefore the static properties of magnetic materials are mainly determined by exchange. However, it can be shown that the influence of dipole–dipole interaction, which is a long-range interaction, becomes important for the dynamical properties at long enough wavelength. Typically, exchange interaction is dominant for spin waves with wavenumber $q > 10^6$ cm^{-1}: this is the exchange region, which includes most of the Brillouin zone and which can be experimentally analysed, at least in the case of bulk specimens, by means of neutron scattering. For smaller values of q, i.e. for larger wavelengths, the dipole–dipole interactions become important, so an intermediate regime can be defined, known as the dipolar–exchange region, in which the exchange and dipolar terms may be comparable. This is the range of wavenumbers probed by BLS experiments. Eventually, for small enough wavenumbers (typically $q < 10^5$ cm^{-1}), dipole–dipole interactions dominate. In this case one can follow a macroscopic approach in terms of Maxwell's equations. A simplification occurs when the inequality $q \ll \omega/c$ holds, where ω is the spin-wave angular frequency and c is the velocity of light. Under such conditions the effects of retardation can be neglected. This defines the so-called magnetostatic region, which typically corresponds to the wavevector range 10 cm$^{-1} < q < 10^5$ cm^{-1}, accessible by FMR experiments. At smaller wavenumbers the full form of Maxwell's equations, including retardation, must be used; this is the electromagnetic or polariton region which can be studied by the attenuated total reflection (ATR) method [20]. However, it is important to emphasize that the ranges of q defined above may vary for different magnetic materials. Moreover, when surface geometries are considered, the interplay between exchange and dipolar effects may sometime be more subtle, so some modes such as standing modes will be much more exchange sensitive than surface modes.

It is important to notice here that, in addition to the exchange and dipole–dipole terms, other contributions must be included in the Hamiltonian of an ordered magnetic material. In particular, there are effects of magnetic anisotropy which can arise because of interactions between the magnetic moments of the atoms and the electric field of the crystal lattice. In the case of layered materials, the broken symmetry of the lattice can introduce additional anisotropy terms, such as the interface anisotropy [21].

4.2. Equation of motion

A model which contains all salient features of spin waves in superlattices including dipolar, exchange, and anisotropy contributions was first proposed for polycrystalline single layers by Rado and Hicken [22] and Cochran and Dutcher [23], and applied to multilayered cubic structures with (100) and (110) orientations by Hillebrands [24, 25] and Stamps and Hillebrands [26–28]. More recently, Gubbiotti *et al* [29] have generalized this model to include magnetic films with the (111) orientation. Here we present the general approach for a
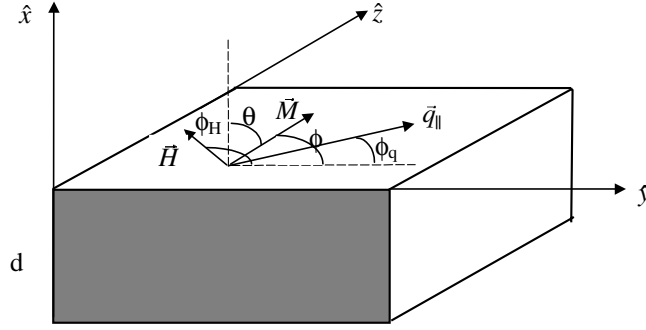
Figure 4. The coordinate system used for calculating spin-wave frequencies, in the case of a magnetic film grown on a semi-infinite substrate.

multilayer of cubic symmetry with explicit anisotropy fields for any of the (100), (110), and (111) orientations.

The geometry for the spin-wave frequency calculation, shown in figure 4, is chosen with the $\hat{x}$-axis perpendicular to the layer. Without loss of generality we choose the $\hat{z}$-axis as the direction of the saturation magnetization, M_s, which is the time-averaged direction of the precessing magnetization, M; θ and ϕ are the polar and azimuthal angles with θ measured from the surface normal. ϕ is measured from a crystallographic reference direction of lowest indices within the film plane (dashed line in figure 4) which is usually [001] for the (100) and (110) orientations while it is [$\bar{1}$10] for the (111) plane. The direction of the spin-wave propagation, defined as that of the wavevector component parallel to the film plane, $q_\parallel$, is within the (y, z) plane. Its angle with the crystallographic reference direction is ϕ_q. The magnetic field is applied parallel to the layer plane, at an angle ϕ_H with respect to the reference direction, and spin wave are considered with $q_\parallel$ always perpendicular to the applied field.

Once the equilibrium direction of the magnetization is determined by a minimization of the total free energy, the spin-wave frequencies are calculated in the usual way from the linearized Landau–Lifshitz torque equation of motion:

$$\frac{\mathrm{i}\omega}{\gamma}\vec{m} = \vec{M} \times \vec{H}_{eff} \tag{2}$$

where ω is the angular frequency and $\vec{m}$ is the magnetization oscillating around its static value $\vec{M}_s$ with $|\vec{m}(t)| \ll |\vec{M}_s|$. In equation (2), $\gamma = \gamma_e g/2$ is an effective gyromagnetic ratio, where $\gamma_e = 1.759 \times 10^7$ Hz Oe^{-1} is the value of γ for the free electron and g is the spectroscopic splitting factor. The effective magnetic field acting on the magnetization, $\vec{H}_{eff}$, is given by

$$\vec{H}_{eff} = \vec{H} + \vec{h} - \frac{1}{M_s}\vec{\nabla}_{\vec{\alpha}}E_{ani} + \frac{2A}{M_s}\nabla^2\vec{M}. \tag{3}$$

The first term on the right-hand side of equation (3) represents the external applied field while the second one is the dipolar magnetic field (generated by precessing spins due to the dipole–dipole interaction) subject to magnetostatic Maxwell equations:

$$\vec{\nabla} \times \vec{h} = 0 \tag{4}$$
$$\vec{\nabla} \cdot (\vec{h} + 4\pi\vec{m}) = 0. \tag{5}$$

The third term of equation (3) is an effective field due to the magnetic anisotropy energy E_{ani} where $\vec{\nabla}_{\vec{\alpha}}$ is the gradient operator for which the differentiation variables are the components of the unit vector $\vec{\alpha}$ pointing in the direction of $\vec{M}_s$. In this article, we do not want

to describe each step of the calculation and therefore the reader is invited to inspect the work of Hillebrands [1] for the (100) and (110) orientations and the extension to the (111) plane constructed by Gubbiotti *et al* [29]. The explicit expressions of both the bulk and the interface anisotropy fields, H_α, H_β, H_γ, $H_{\alpha'}$, $H_{\beta'}$, $H_{\gamma'}$, entering the calculation are also provided there.

The appropriate boundary conditions have then to be applied and the problem must be solved numerically. Selected simulations of spin-wave modes in thin films and multilayers, calculated using the above-described numerical procedure, are found in [2].

4.3. Analytic expression for ultrathin films

When dealing with ultrathin magnetic films, whose thickness is below the exchange–correlation length, typically a few nanometres, the complexity of the numerical calculation can be overcome by use of a more straightforward analytical procedure. The magnetization is assumed to be uniform across the magnetic film. (The problem of the angular variation in the static magnetization near the surface of a thick film has been treated by Mills [30] and by O'Handley and Woods [31].) In this condition, the product of the film thickness d and the wavevector $q_\parallel$ is small compared to unity and the frequency of the spin wave for an in-plane-magnetized sample can be expressed as

$$
\left(\frac{\omega}{\gamma}\right)^2 = \left(H\cos(\phi_H - \phi) + H_\alpha + \frac{2}{d}H_{\alpha'} + \frac{2A}{M_s}q_\parallel^2 + 4\pi MD(1 - q_\parallel d/2)\right)
$$
$$
\times \left(H - \cos(\phi_H - \phi) + H_\beta + \frac{2}{d}H_{\beta'} + \frac{2A}{M_s}q_\parallel^2 + 2\pi MD q_\parallel d\right)
$$
$$
- \left(H_\gamma + \frac{2}{d}H_{\gamma'}\right)^2. \tag{6}
$$

The parameter D comes from the demagnetizing tensor, which depends on the shape of the specimen and on the direction of the applied magnetic field [32]. For a thin film all tensor elements are zero except for that in the direction perpendicular to the layer. In this case one has $D = 1$ for a film of at least three to four monolayers. In the case of thinner films it should not be considered as a continuum, but has to be treated as a set of discrete magnetic dipoles on a regular lattice. For instance, analytical calculations show that the correct expression for the demagnetizing factor for a (100) fcc film is $D = 1 - 0.2338/n$ with n the number of monolayers [33]. Since the magnetization is uniform across the film, the interface torques from the interface anisotropies are converted into volume torques acting on the entire film magnetization, and the interface anisotropy fields are converted into effective volume anisotropy fields weighed by $2/d$, with the factor of two counting the two interfaces of the film. Equation (6) contains both the volume and the interface anisotropy fields and it can be easily applied to Brillouin scattering experiments. The spin-wave frequency calculated using this approximation corresponds to the so-called Damon–Eshbach (DE) surface [34] mode which is also present on the surface of a semi-infinite medium.

4.4. Out-of-plane-magnetized films

In the case of ultrathin films, it may happen that the equilibrium direction of the magnetization is perpendicular to the film surface, because of the presence of a strong enough perpendicular magnetic anisotropy. The calculation of the spin-wave frequency for perpendicularly magnetized films has been reported by Stamps and Hillebrands [35] including the effects of both dipolar and exchange interactions. Here we present the main features of their model, taking into account both bulk and surface magnetic anisotropy. The magnetization is assumed
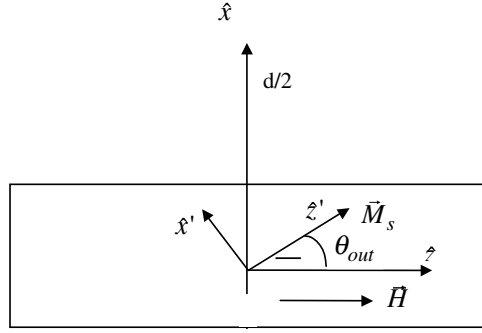
Figure 5. Coordinate reference systems used for the calculations of the spin-wave frequency for out-of-plane-magnetized films. The unprimed coordinate system is with the x-axis normal to the film plane. The applied field H is taken along the z-axis and the saturation magnetization M_s lies in the xz-plane. A primed coordinate system is defined such that M_s lies along the z'-axis. The angle θ_{out} is defined between the z'- and z-axes.

to have a generic orientation with respect to the film plane, because of the presence of a strong out-of-plane magnetic anisotropy, which overcomes the demagnetizing field, which tends to align the magnetization along the film plane. Since the spin waves probed by the BLS technique have wavelength comparable with that of light, i.e. much larger than the lattice parameters, the medium can be considered as a continuum and the discrete nature of the spins can be neglected. The geometry for the spin-wave dispersion calculation was chosen with the $\hat{x}$-axis normal to the film surfaces and the $\hat{z}$-axis along the direction of the external field H, as shown in figure 5.

In order to simplify the expression for the Landau–Lifshitz equation of motion, a second coordinate system, called the primed frame, is defined with the $\hat{z}'$-axis parallel to the saturation magnetization, at an angle θ_{out} from the $\hat{z}$-axis. Please note that in this case the polar angle θ_{out} is measured with respect to the film plane. The total anisotropy energy density of an uniformly magnetized material can be represented, to a first-order approximation, as

$$E_{ani} = -K_{eff}^{(2)} \sin^2 \theta_{out} - K_{eff}^{(4)} \sin^4 \theta_{out} \tag{7}$$

where θ_{out} is the angle between the magnetization and the in-plane $\hat{z}$-axis, while $K_{eff}^{(2)}$ and $K_{eff}^{(4)}$ are the second- and fourth-order effective anisotropy constants. In many cases it is possible to neglect the fourth-order constant, so $K_{eff}^{(2)}$ includes all relevant anisotropy energy density contributions which determine the magnetization orientation in epitaxial magnetic films:

$$K_{eff}^{(2)} = -2\pi M_s^2 + \left(K_V + \frac{2k_s}{d} \right). \tag{8}$$

The first term of $K_{eff}^{(2)}$ is the shape contribution, which is responsible of the in-plane orientation of the magnetization at large film thicknesses. M_s is the saturation magnetization. K_V and k_s are the volume and interface magnetocrystalline anisotropy constants, respectively; these can be justified in terms of a phenomenological model first proposed by Néel [21]. K_V includes contributions of different origin, such as magnetocrystalline and magnetoelastic (ME) anisotropy. The magnetic free energy per unit area, including the potential energy density of the magnetization in the external field, assumes the following form:

$$F/\sigma = \int [-HM_s \cos \theta_{out} + 2\pi M_s^2 \sin^2 \theta_{out} - K_V \sin^2 \theta_{out}] \, \mathrm{d}x - 2k_s \sin^2 \theta_{out} \tag{9}$$

where the factor 2 in the last term accounts for the two interfaces of the magnetic film. Because we are considering ultrathin magnetic films with thickness lower than the exchange–correlation

length, the magnetization can be assumed to be approximately uniform across the film thickness and therefore independent of the x-coordinate. This makes possible the definition of a magnetic free energy per unit volume in the form

$$F/V = -HM_s \cos \theta_{out} - K_{eff}^{(2)} \sin^2 \theta_{out}. \tag{10}$$

The minimum of F/V with respect to θ_{out} gives the equilibrium direction of the magnetization defined by θ_{out}. One solution is always $\theta_{out} = 0$. Another possible solution is obtained for

$$\cos \theta_{out} = HM_s/2K_{eff}^{(2)}. \tag{11}$$

In the limit of zero applied field the equilibrium direction of the magnetization is normal to the film plane ($\theta_{out} = \pi/2$) for $K_{eff}^{(2)} > 0$ and parallel to the film plane ($\theta_{out} = 0$) for $K_{eff}^{(2)} < 0$.

In the presence of a large out-of-plane anisotropy, equation (11) predicts that the magnetization lies out of the plane for zero applied field, while it begins to rotate in the film plane under the action of the field. A critical field H_{crit} can be defined such that for $H > H_{crit}$ the magnetization lies in the film plane. The expression for this critical field, which follows from equation (11) with $\cos \theta_{out} = 1$, is as follows:

$$H_{crit} = \frac{K_{eff}^{(2)}}{M_s}. \tag{12}$$

Figure 6 shows the calculated values for the angle θ_{out} as a function of the external applied field in the case of a Co film for a positive value of $K_{eff}^{(2)}$. Here the parameters are appropriate for Co, with $4\pi M_s = 17.6$ kOe, $d = 0.6$ nm, and $k_s = 0.4$ erg cm^{-2}. The volume anisotropy constant K_V has been set to zero for simplicity. Using these parameters, the calculated value of the critical field is 1430 Oe. For zero applied fields, $\theta_{out} = 90°$, indicating an out-of-plane magnetization orientation, and then θ_{out} reduces when the field intensity is increased. For fields higher than H_{crit} the angle θ_{out} is zero, indicating that the magnetization has been forced to lie in the film plane. It is worth noticing that if the fourth-order term was not neglected in equations (7) and (10), a canted ground state for the magnetization could be found [36]. Instead, the presence of the second-order term, alone, allows the magnetization to be either in the film plane or perpendicular to it for zero applied field.

Once the direction of the magnetization has been determined, the spin-wave frequency can be calculated by use of a standard procedure which relies upon the resolution of the Landau–Lifshitz equation of motion in the magnetization frame, imposing both the electromagnetic and the Rado–Weertmann boundary conditions at the film interfaces [37]. Since the surface anisotropy fields are described by effective bulk anisotropy fields, changes in spin-wave frequencies from different surface anisotropies at the top and bottom surfaces of the film cannot be considered in this theory. This is a significant limitation of the present theory as compared to the theoretical model used for in-plane-magnetized films. In the case of perpendicular magnetization, the positive sign of H_{crit} has an important consequence for the spin-wave frequency dependence on the applied-field strength. This can be seen in figure 7 where the spin-wave frequency is calculated for a Co film using the same magnetic parameters as reported above. With increasing field, H, the spin-wave frequency first decreases while the direction of magnetization is increasingly tilted into the layer plane. At $H_{crit} = 1430$ Oe the magnetization lies in the plane and for further increasing fields, the spin-wave frequency increases in a nearly linear fashion, as is characteristic of in-plane-magnetized samples.

5. Selected applications

In the following, a few examples will be given of the investigation of the magnetic properties of low-dimensional systems, mainly performed at GHOST laboratory [14], Perugia University,
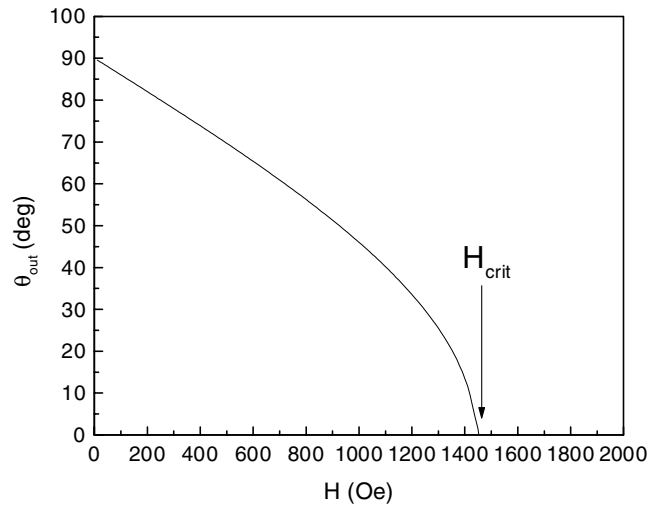
Figure 6. The calculated value of the angle between the magnetization and the applied field as a function of its strength for a Co film 0.6 nm thick. The magnetic parameters used for the calculation are reported in the text.
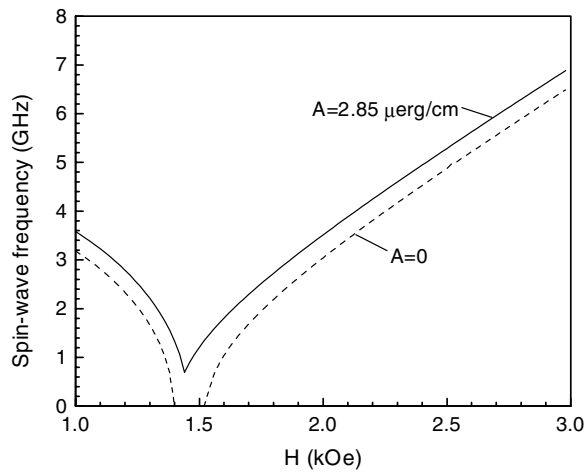

Figure 7. Spin-wave frequency as a function of the applied magnetic field for the surface mode with (full curve) and without (dashed curve) exchange for a 0.6 nm thick Co film. The interface anisotropy constant is $k_s = 0.4$ erg cm^{-2} while the volume anisotropy constant has been set to zero for simplicity.

by the combined use of BLS and the SMOKE. The investigations reviewed will be concerned with interface anisotropy, in-plane and out-of-plane anisotropy in ultrathin films, as well as with spin waves in patterned arrays of magnetic dots. Other interesting problems where the combined use of BLS and the SMOKE has been successfully exploited will not be discussed here. Among them we mention the study of interlayer coupling in magnetic/non-magnetic multilayers [38, 39] and analysis of spring magnets consisting of hard/soft-magnetic layers [40, 41].

5.1. Fe/Cu/Si(111)

Metal–metal epitaxy on silicon (MMES) has been exploited in order to grow high-quality magnetic films of Fe on a Si substrate, through the introduction of a Cu buffer layer [42]. Epitaxial Fe films, with thickness in the range between 2.5 and 110 Å, were prepared at Camerino University in a UHV system, with a base pressure of 2×10^{-11} Torr, equipped with standard preparation and characterization facilities such as those for low-energy electron diffraction (LEED), Kikuchi electron diffraction (KED), and Auger electron spectroscopy (AES) [43]. The substrate was an optically polished Si(111) crystal (p-type, $0.1\,\Omega$ cm) clamped on two rods for direct Joule heating. After the preparation of a good quality 7×7 reconstruction of the Si(111) surface, a 35 Å thick Cu buffer layer was used to avoid the formation of Fe silicides and/or metallic islands. In addition, a 35 Å thick Cu protective overlayer was grown on top of the Fe films to prevent oxygen contamination during *ex situ* measurements and to achieve identical interfaces on either side of the Fe film. Concerning the growth of the Cu buffer layer, it has been shown elsewhere using LEED and KED [44–46] that, because of the large mismatch with Si, pseudomorphism never occurs and the Cu growth mode follows the so-called 'cube-on-cube growth', i.e. Cu grows with its own bulk lattice parameter and with the (111) orientation induced by the Si substrate. In particular, the Cu buffer layer consists of twinned islands producing sixfold-symmetric LEED and KED patterns, unlike the threefold symmetry patterns expected for a Cu(111) single crystal. The structural properties of the Fe layers were studied by means of an accurate analysis of the LEED patterns, showing that up to a thickness of about 6 Å a fcc Fe layer, pseudomorphic to the Cu buffer, is obtained. For a Fe coverage of 6 Å or higher, one observes the growth of three-dimensional domains of bcc Fe(110) in the Kurdjumov–Sachs (KS) orientation [47–50] on the hexagonal net of pseudomorphic Fe on Cu(111).

Normalized SMOKE longitudinal hysteresis loops, measured at room temperature, for Fe films with thickness between 110 and 4 Å are shown in figure 8. For Fe films thicker than 6 Å, the loop remanence is relatively large, as is characteristic of easy-M–H loops, whereas the loops taken with the applied field normal to the film plane, which are not shown here, exhibit a linear behaviour and an insignificant remanence. This indicates that the magnetization easy axis lies in the film plane, in agreement with the expected in-plane alignment of the magnetization at sufficiently large film thicknesses, due to the predominant contribution of the magnetostatic term in the magnetic free energy. For Fe films thinner than 6 Å, no hysteresis loop could be detected either in the longitudinal or the polar geometry at room temperature because of the low value of the Curie temperature. However, low-temperature (<50 K) measurements show that these films are ferromagnetic, with the magnetization orientation perpendicular to the film plane [51].

The analysis of the longitudinal Kerr intensity, reported in figure 9, revealed that two different ranges of Fe thickness can be identified, lower and higher than ≈ 10 Å, each of them characterized by a roughly linear behaviour with different slopes. This change of slope happens in the thickness range where the structural fcc–bcc transformation has been observed and can be interpreted as due to the presence of an fcc phase of iron with lower magnetic moment with respect to the bcc phase, i.e. a different value of the saturation magnetization [52, 53]. This value can be estimated to be about three times smaller than that corresponding to the bcc Fe phase, in agreement with previous results of Gradmann *et al* [54]. The observed behaviour also provides experimental confirmation that the Kerr signal depends linearly on the thickness of the Fe layer as long as the film thickness is lower than the light penetration depth. A saturation effect is only observed for Fe thicknesses larger than 70 Å, in agreement with the observation made by Qiu *et al* [55] for ultrathin Fe(110) films.
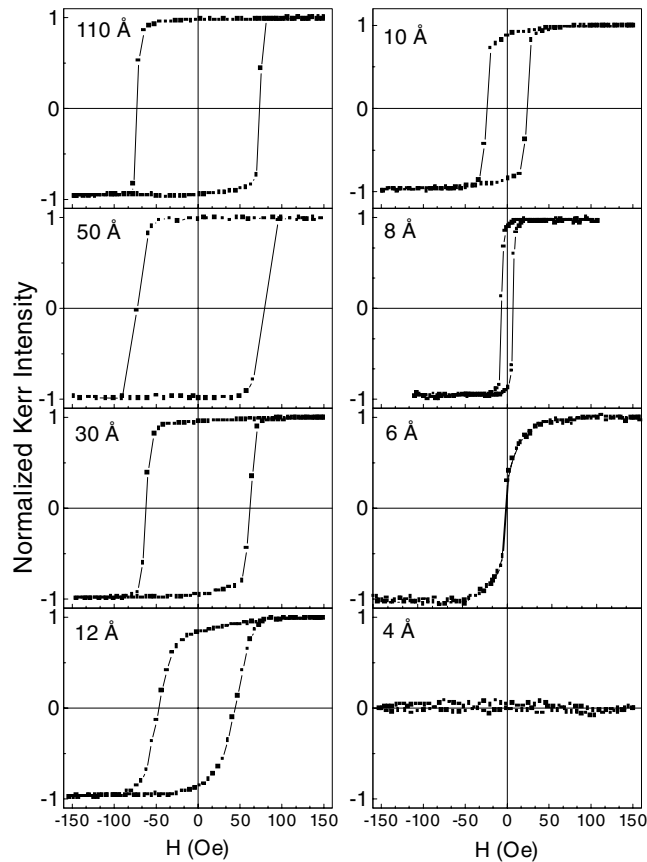
Figure 8. Room temperature longitudinal SMOKE loops for Fe films whose thicknesses are reported in the figure. The external field intensity varies in the range -150 to $+150$ Oe. From [42].

From a quantitative analysis of the SMOKE loops it was possible to determine the behaviour of the coercive field H_{coerc} which is plotted in figure 10 as a function of the Fe film thickness. H_{coerc} exhibits a sudden increase for thicknesses higher than 6 Å, i.e. simultaneously with the structural fcc-to-bcc transition, reaching a constant value of about 70 Oe for thicknesses above 50 Å. It was previously shown that this structural transformation is accompanied by the appearance of three-dimensional islands in the KS orientation upon the first pseudomorphic Fe layers. It is equally well known that island formation and disorder in magnetic systems increase the coercive field [56]. These two arguments taken together allow one to interpret the rapid rise in the coercive field versus Fe film thickness as being due the increasing disorder associated with the island growth and we can therefore take the onset thickness of the rapid increase in H_{coerc} as an estimate of the critical thickness (≈ 6 Å) above which the fcc–bcc transition occurs.

As a second step of the SMOKE characterization, high-field polar loops were carried out to saturate the film along the normal to the surface (x-axis in figure 5) and to determine the value of the out-of-plane anisotropy constants. The sequence of experimental SMOKE loops is presented in figure 11. From a direct observation of the loops one can see that the saturation field is lower than that expected from shape anisotropy alone, assuming the bulk
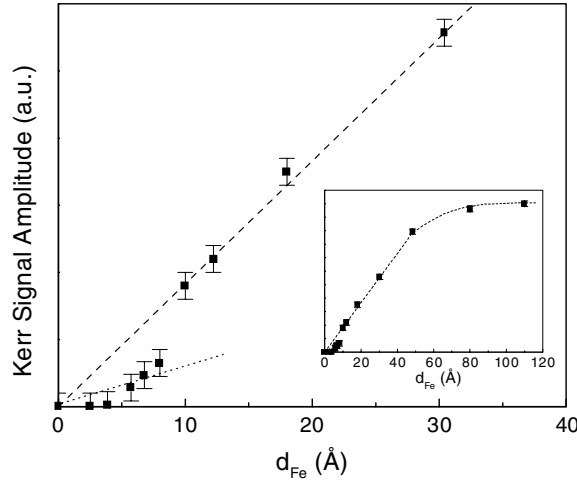
Figure 9. Kerr signal amplitude in the longitudinal configuration as a function of Fe film thickness. It can be seen that two regimes of almost linear behaviour can be identified, characterized by different slopes. The inset shows that for Fe thicknesses larger than 70 Å a saturation of the Kerr signal is observed because of the finite penetration depth of light. From [42].
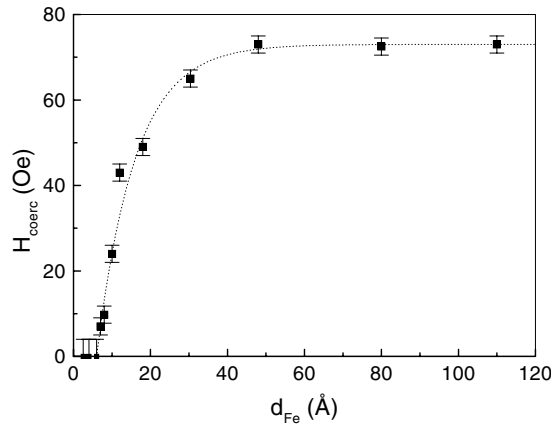

Figure 10. The thickness dependence of the coercive field of the longitudinal M–H loops. The dotted curve is a guide to the eye. From [42].

bcc value $4\pi M_s = 21$ kOe. This indicates a positive (i.e. out-of-plane) contribution from the uniaxial anisotropy. Concerning the loop shape, there is a predominantly linear approach to the saturation, due to the second-order anisotropy, followed by a slight curvature for high magnetic fields caused by the presence of a second-order anisotropy term. Therefore, the general expression for the magnetic free-energy density can be written as [57]

$$E = -K_{eff}^{(2)} \cos^2 \theta_N - K_{eff}^{(4)} \cos^4 \theta_N - M_s H \cos \theta_N \qquad (13)$$

where $\theta_N = \pi/2 - \theta_{out}$ is the angle between the magnetization and the film normal (which now coincides with the applied-field direction), and $K_{eff}^{(2)} \cos^2 \theta_N$ and $K_{eff}^{(2)} \cos^4 \theta_N$ represent the second- and fourth-order anisotropy energy terms, respectively. The last term describes
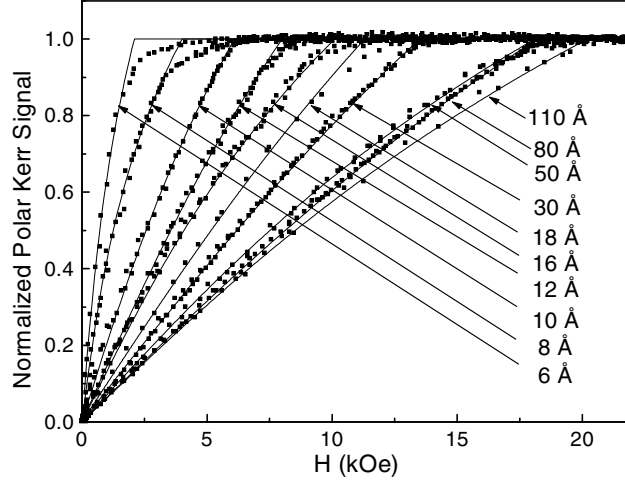
Figure 11. Experimental magnetization data in the polar SMOKE configuration for Fe films with different thicknesses. The continuous curves are calculated by a best-fit procedure. Adapted from [42].

the interaction between the external applied field and the magnetization. The equilibrium magnetization orientation as a function of the magnetic field strength is given by

$$\cos(\theta_N^{eq}) = \frac{H}{H_{sat}^{(2)} + H_{sat}^{(4)} \cos^2 \theta_N^{eq}} \tag{14}$$

where $H_{sat}^{(2)} = -2K_{eff}^{(2)}/M_s$ and $H_{sat}^{(4)} = -4K_{eff}^{(4)}/M_s$ are the second- and fourth-order saturation fields, respectively. A quantitative determination of $H_{sat}^{(2)}$ and $H_{sat}^{(4)}$ (see figure 12) has been obtained from a best fit of the experimental data to the calculated magnetization curves; it shows that the main contribution to the magnetic energy comes from the first-order anisotropy, the second-order anisotropy constants being appreciably smaller, if not negligible, as shown in figure 13. This results are in agreement with a previous investigation on Fe-based multilayers [58]. In order to achieve a deeper insight into the physical meaning of the anisotropy constants, it is useful to subtract the shape anisotropy energy from the first-order anisotropy and distinguish between a bulk and an interface contribution. One has

$$H_{sat}^{(2)} = -\frac{2K^{eff(2)}}{M_s} = -\frac{2}{M_S}\left(-2\pi M_S^2 + K_V + 2\frac{k_s}{d}\right) = 4\pi M_S - \frac{2K_V}{M_S} - 4\frac{k_s}{dM_s}. \tag{15}$$

In figure 14 the behaviour of $K_V d + 2k_s$ is plotted as a function of the film thickness d. A linear behaviour is observed, and the intrinsic volume and interface anisotropy constants, K_V and k_s, correspond to the slope and the intercept of the linear regression curve, respectively. The positive sign of these anisotropy constants indicates that the intrinsic anisotropy favours the magnetization easy axis being perpendicular to the film plane. In addition, the value K_V is rather different, five times greater than the magnetocrystalline volume anisotropy for bulk Fe [59], indicating that some additional contributions such as that from ME anisotropy come to play a significant role in determining the magnetic anisotropy.

In order to perform a direct quantitative comparison between the results from the SMOKE and BLS techniques, the latter technique has been used to analyse magnetic anisotropy in the same films. The anisotropy contributions, which are sources of additional effective fields in the ferromagnetic film, are felt by the precessing spins and can be derived from a measurement of the spin-wave frequency as a function of either the applied magnetic field or the film
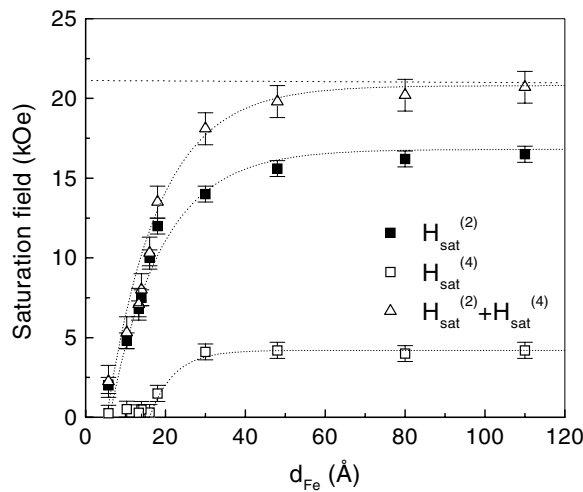
Figure 12. Behaviour of the second-order, fourth-order, and total saturation fields determined by a best fit to the experimental polar loops for Fe films of different thicknesses. Adapted from [42].
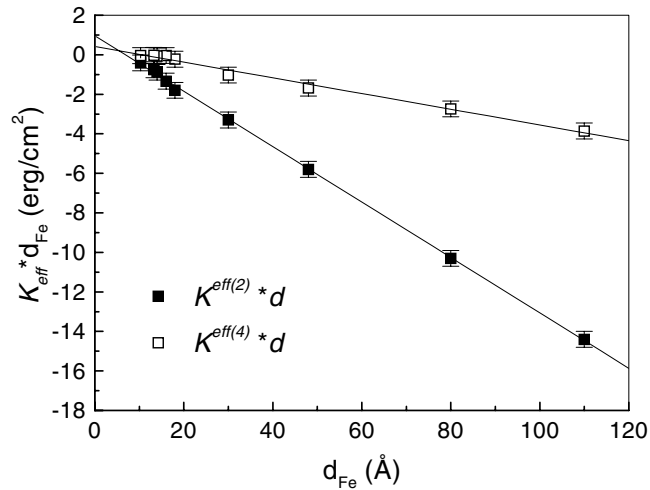

Figure 13. Behaviour of the second- and fourth-order effective magnetic anisotropies as a function of Fe layer thickness. Adapted from [42].

thickness. Figure 15 shows a sequence of experimental BLS spectra relating to films with different thicknesses, for an external field of 1 kOe. In addition to the dominant peak due to elastically scattered light, the Damon–Eshbach mode is clearly observed at frequencies in the range 3–21.5 GHz. This is the only peak present in BLS spectra, because the ratio between the film thickness and magnon wavelength is so low that bulk standing modes are at very high frequencies, not accessible in our experiments. The DE peaks exhibit a remarkable Stokes–anti-Stokes asymmetry, caused by the elliptical spin precession, typical of magnons in thin ferromagnetic films of absorptive materials [60]. A study of the frequency dependence of the DE mode on the magnetic field strength has been carried out for all the Cu/Fe/Cu/Si(111) heterostructures with Fe thickness larger than 6 Å, i.e. characterized by a practically constant value of the saturation magnetization. The experimental data relating to the frequency of the
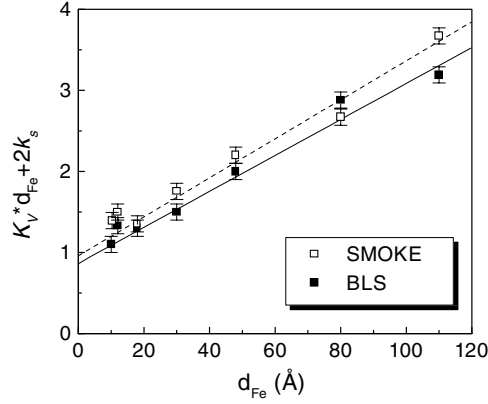
Figure 14. Experimental values of the intrinsic uniaxial anisotropies determined by the SMOKE (open squares) and the BLS technique (full squares) versus the Fe layer thickness. The straight line is the result of a linear least-squares fit to the data based upon the model described in the text. From [42].
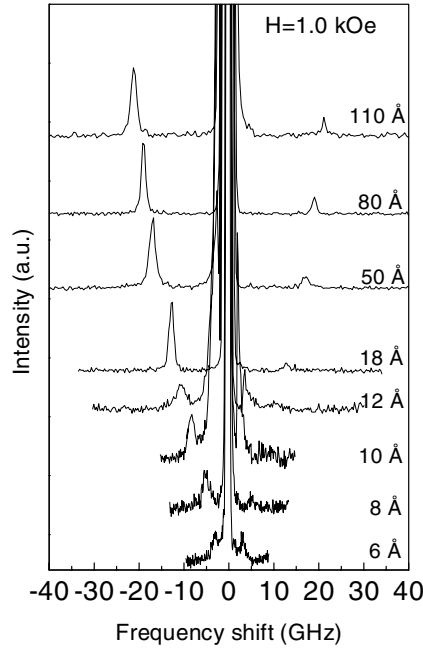

Figure 15. Room temperature Brillouin spectra of epitaxial Cu/Fe/Cu/Si(111) heterostructures with different thicknesses of the Fe film for an external field of 1.0 kOe, applied in the film plane. From [42].

DE peak have been fitted to the curves calculated by using the following analytical expression, which is a specialization of equation (6) to the case of a uniaxial anisotropy:

$$
\left(\frac{\omega}{\gamma}\right)^2 = \left(H + \frac{2A}{M_s} q_\parallel^2 - \frac{2}{M_s}\left(K_V + \frac{2k_s}{d}\right) + 4\pi D M_s (1 - q_\parallel d/2) \right)
$$
$$
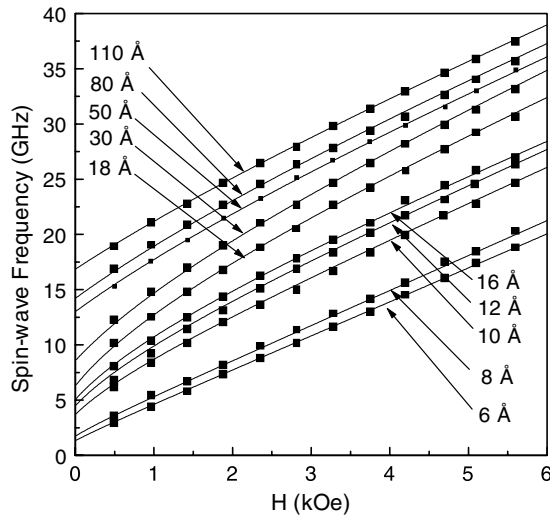\times \left(H + \frac{2A}{M_s} q_\parallel^2 + 2\pi D M_s q_\parallel d \right). \tag{16}
$$

Figure 16. Magnetic field dependence of the DE surface mode frequency for Cu/Fe/Cu/Si(111) heterostructures with Fe thicknesses in the range between 6 and 110 Å. Continuous curves are obtained by a best-fit procedure using the analytical expression for the spin-wave frequency in the ultrathin-film approximation. From [42].

Both the experimental frequencies and the fitting curve are reported in figure 16. Qualitatively, the almost linear dependence of the spin-wave frequency on the applied field, with extrapolated positive intercept on the frequency axis, indicates that all these samples are in-plane magnetized, as already shown by SMOKE measurements. Quantitatively, from a procedure for obtaining the best fit of the calculated curves to the experimental points, the values of the spectroscopic separation factor g and of the anisotropy constant $K_V d + 2k_s$ were obtained for each specimen, taking the exchange constant and the saturation magnetization fixed at their values for bcc iron: $A = 2.0$ μerg cm^{-1} and $4\pi M_s = 21.0$ kOe. In this way, $g = 2.17 \pm 0.03$ was obtained, which is in good agreement with the result previously found for Fe films by the BLS technique [61]. As regards the anisotropy constants, the behaviour of $K_V d + 2k_s$ as a function of d is plotted in figure 14 together with those previously determined from the first-order SMOKE data (open squares). From a linear regression of the BLS data we obtained $K_V = (2.2 \pm 0.2) \times 10^6$ erg cm^{-3} and $k_s = (0.43 \pm 0.02)$ erg cm^{-2} which compare very well with the first-order SMOKE results ($K_V = (2.4 \pm 0.1) \times 10^6$ erg cm^{-3} and $k_s = (0.48 \pm 0.03)$ erg cm^{-2}). Both the BLS and the SMOKE technique yield a positive sign of the intrinsic anisotropy, indicating that the surface normal is a magnetic easy axis for this anisotropy contribution. FMR measurements previously performed by Heinrich *et al* [62] on epitaxial Cu/Fe(001)/Au trilayers, gave the same sign for the interface anisotropy constant, but larger magnitude (0.62 erg cm^{-2}), owing presumably to the different crystallographic orientation and to the exposure of one Fe surface to Au rather than both to Cu.

In order to better clarify the role of interface anisotropy, in figure 17 the behaviour of the DE mode frequency as a function of the Fe film thickness is plotted, for a constant value of the applied magnetic field of 1.0 kOe. It can be seen that the agreement between the experimental data and the theoretical curve, calculated with the parameters obtained from the fitting procedure described above, is quite satisfactory. In particular, the frequency reduction observed below 30 Å is due to the influence of the out-of-plane interface anisotropy constant k_s. In this range of thicknesses the DE surface mode becomes an interface-anisotropy-dominated
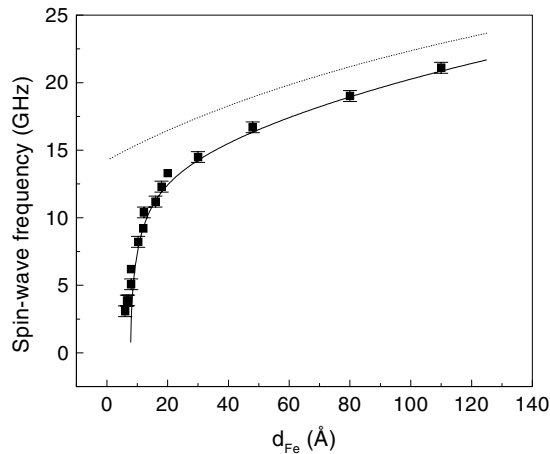
Figure 17. Frequency dispersion of the DE surface mode versus Fe film thickness for an applied field of 1 kOe. The continuous curve is a fit to the experimental data, while the dotted curve is the behaviour expected for the DE mode without considering exchange interaction and interface anisotropy. From [42].

mode, as expected from the $1/d$ dependence of the interface anisotropy contribution. For the sake of comparison, the behaviour of the DE mode calculated in the absence of any interface anisotropy (dotted curve) is also reported in the same figure. Note that for Fe thicknesses lower than 10 Å a slight discrepancy between the spin-wave frequency and the calculated curve is observed. This deviation, which occurs just in the region where the structural transformation of iron takes place, can be attributed to the reduced magnetic moment of the fcc phase of iron already evidenced by the SMOKE measurements.

5.2. Epitaxial Ni/Cu/Si(100): perpendicular anisotropy and the role of domains

Epitaxial Cu/Ni/Cu/Si(001) films present a collinear phase magnetized perpendicularly to the film plane for a wide range of Ni thickness, 17–120 Å [36, 63, 64].

In an effort to understand this perpendicular phase more fully, the magnetic properties of epitaxial Cu/Ni/Cu/Si(001) films, deposited in a molecular-beam epitaxy (MBE) chamber by electron-beam evaporation, have been investigated by means of magneto-optical vector magnetometry and BLS [65–67]. Ni films with thickness in the range $17 < d_{Ni} < 120$ Å were deposited at room temperature on Si(001) substrates using a 2000 Å thick Cu buffer layer and covered by a 50 Å thick Cu protective film. In figure 18 the polar Kerr loops taken at room temperature with a magnetic field applied perpendicularly to the film are reported. The high values of the remanent magnetization indicate that, within this range of thickness, the films present a uniform perpendicular magnetization. BLS experiments were performed with a dc magnetic field, variable between 1.5 and 16 kOe, applied in the film plane and normal to the incidence plane of light. The light source used for the BLS experiment was a p-polarized single-mode Ar^+-ion laser with an emission wavelength of 5145 Å and typical output power of 200 mW.

Assuming a collinear spin configuration, the magnetization, parallel to the perpendicular axis in zero field, rotates towards the in-plane direction as the field is increased until, for a critical value H_{crit} of the magnetic field, it falls completely within the film plane, as outlined in section 4.4. The theoretical field dependence of the uniform mode frequency, as expected on
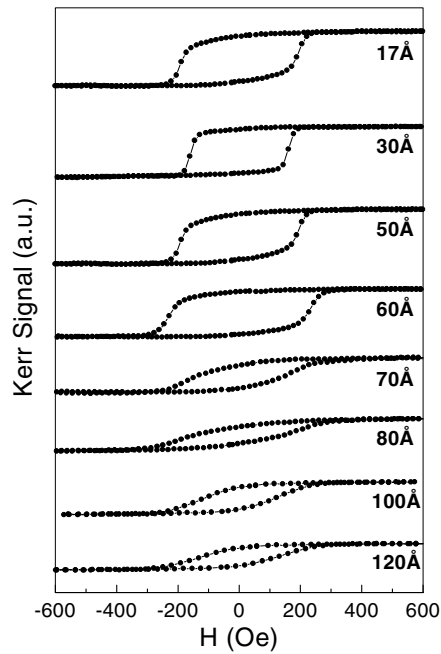
Figure 18. Polar Kerr loops at different thicknesses, taken at room temperature applying a magnetic field perpendicularly to the film. From [65].

the basis of a collinear spin configuration, is shown in figure 19 by the full curve: a minimum is predicted just for $H = H_{crit}$. Such a behaviour was indeed observed in many systems with perpendicular magnetization [68]. In contrast, the BLS data for the field dependence of the uniform mode, displayed by square symbols in figure 19, show a monotonic behaviour. The measured frequency is in agreement with the theoretical curve only as far as the linear field dependence in the in-plane phase (full line, $H > H_{crit}$) is concerned; as the field is decreased, a clear change in the slope of the frequency versus H is observed. A monotonic decrease is found down to $H = 1.5$ kOe, when the peak for the Brillouin spectra merges with the central line. The origin of this discrepancy between theory and experiment can been attributed to the formation of stripe domains with the magnetization pointing up and down with respect to the film surface [67].

In order to estimate the value of the effective anisotropy constant $K_{eff}^{(2)}$, defined according to equations (7) and (12), the critical field H_{crit} has been obtained by a best-fit procedure, fitting the measured spin-wave frequencies to those calculated in the high-field region, where the magnetization is in the film plane. In addition, the values of the saturation magnetization for the Ni film with different thicknesses have been measured by VSM [66]. The values of $K_{eff}^{(2)}d_{Ni}$ obtained for the Cu/Ni/Cu/Si(001) films by the BLS technique are reported in figure 20, where, for the sake of comparison, previous results obtained by torque magnetometry (TM) [36][1] are also shown. Excellent agreement was found between the values of $K_{eff}^{(2)}d_{Ni}$ determined by the two techniques. Both the BLS technique and TM yield a positive sign up to a thickness of 120 Å, indicating that the films have a significant component of magnetization perpendicular to the film surface. For larger thickness a reorientation transition occurs because of the strong

---

[1] Please note that, comparing with the paper of Ha and O'Handley [36], one has to take into consideration the different definitions of the magnetic free energy and of the reference angle of the magnetization with respect to the film plane.
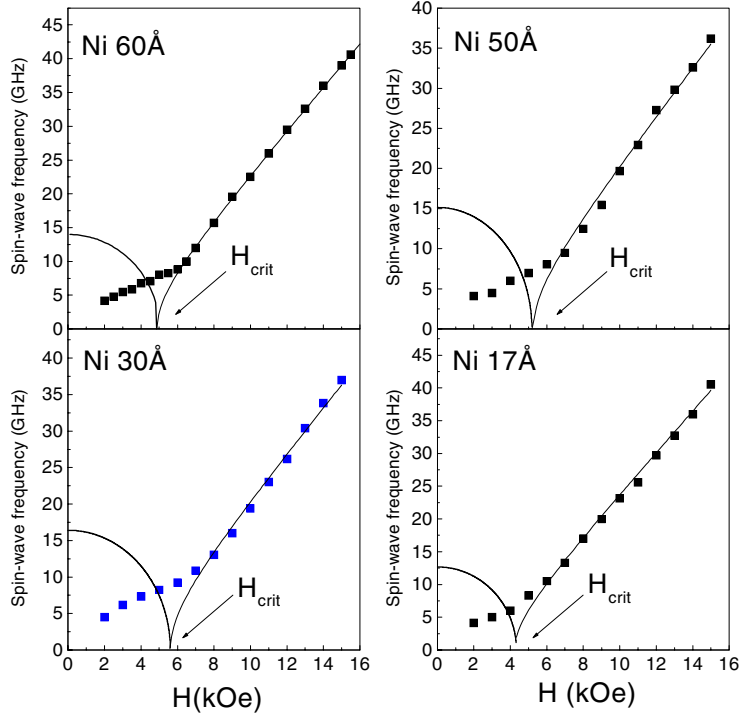
Figure 19. Squares: BLS data for the spin-wave frequency versus the in-plane magnetic field. Full curves: standard spin-wave theory, predicting a minimum at H_{crit}. From [65].

shape anisotropy which aligns the magnetization in the film plane. The dependence of the magnetic anisotropy energy on the Ni film thickness (d_{Ni}) has been fitted using an expression which splits out the bulk and interface magnetic anisotropy contributions:

$$K_{eff}^{(2)}d_{Ni} = 2(K_N + B_I + D_I\varepsilon_0) + \left[B_1\left(1 + \frac{2c_{11}}{c_{12}}\right) - D_B\varepsilon_0\right]\varepsilon_0 d_{Ni} - 2\pi M_s^2 d_{Ni}. \qquad (17)$$

Here, K_N is the Néel-type term due to the copper/nickel interaction at the interface, B_I is the linear interface ME coefficient, D_I is the second-order interface ME coefficient, B_1 is the linear bulk ME coefficient, D_B is the effective second-order bulk ME correction which is included due to the strong internal strain, M_s is the saturation magnetization, c_{11} and c_{12} are elastic constants of Ni, and ε_0 is the biaxial in-plane strain which has been found to show a phenomenological $(1/d_{Ni})^{2/3}$ power dependence. In equation (17), K_N and D_B are the adjustable parameters while for B_I and D_I the values obtained by means of the spin-pair model, $B_I = -1.22$ erg cm^{-2}, $D_I = -1.94$ erg cm^{-2} [69], are used in the analysis of the data. Thus, the values obtained from the fitting procedure are $K_N = (0.72\pm0.06)$ erg cm^{-2} and $D_B = (0.87\pm0.08) \times 10^9$ erg cm^{-2}. These are in good agreement (i.e. within the experimental error) with those obtained by Ha and O'Handley [69] from the torque data ($K_N = 0.72$ erg cm^{-2} and $D_B = 1.1 \times 10^9$ erg cm^{-2}).

In order to have a direct confirmation of the presence of domains below H_{crit} in the Ni samples, the recently developed MOKE–vector magnetometry (MOKE–VM) technique was employed. MOKE–VM loops were recorded in air with the applied field in the film plane using a set-up for magneto-optical ellipsometry based on the photoelastic modulation technique for the modulation of polarization. This technique allows the determination of the magnetization vector orientation versus the applied external field. Figure 21 shows the MOKE–VM loops,
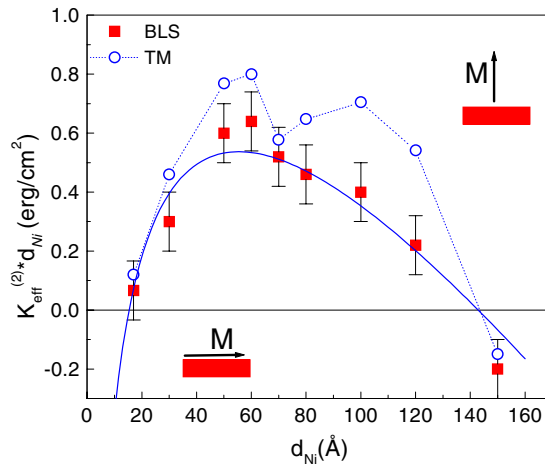
Figure 20. Comparison between the magnetic anisotropy energies deduced by the BLS technique and TM. The full curve is the fitting of the BLS data obtained using equation (17). From [66].

normalized to the saturation signal, obtained from the 50 Å thick Ni film, where the external field H is swept in the film plane. The measurements show a distinctive component of magnetization perpendicular to the film plane during the magnetization switching. The figure shows also the plot of the magnetization modulus as a function of field. For $H < 6$ kOe (just the order of magnitude of the critical field H_{crit}), one can observe $|M| < 1$. The reduction of the modulus means that the magnetization vector is no longer defined, indicating that the magnetization reorientation is accompanied by the formation of domains. Indeed, if there is no domain formation, $|M| = 1$ independently of H. This supports the conclusion that the disagreement between experimental results and the theoretical prediction for the field dependence of the uniform mode frequency is due to the domain formation for the out-of-plane component, while the in-plane one is along the field direction. On the basis of the MOKE–VM data one can also expect the frequency of the uniform mode to decrease monotonically as H goes to 0 [67].

Finally, to reveal the possible occurrence of a canted magnetization, the MOKE–VM technique was also exploited in a canted-field geometry. The field was applied within the plane formed by [001], the normal to the film, and [110], the in-plane easy axis; the field direction formed a canting angle θ_H with the perpendicular axis. In figure 22 such MOKE–VM data are shown for the polar and the longitudinal components of the magnetization, respectively. The different curves refer to different orientations of the applied magnetic field, ranging between $0°$ and $20°$. The perpendicular component M_{polar} shows a remanence in zero field, greater for lower θ_H. Also the parallel component M_{long} is found to be non-zero in zero applied field; moreover, when the applied magnetic field was sufficiently high ($|H| > 4$ kOe), M_{long} was found to decrease with increasing H for θ_H lower than about $11°$ and to increase for $\theta_H = 20°$. Therefore, these observations call for a canted ground-state configuration in zero field with a canting angle between $11°$ and $20°$. As regards the magnetization modulus, it was always decreasing as the field was decreased, mainly owing to the decrease of the M_{polar}-component. This is a strong evidence for a slightly canted ground state with a domain structure for the perpendicular component of the magnetization.
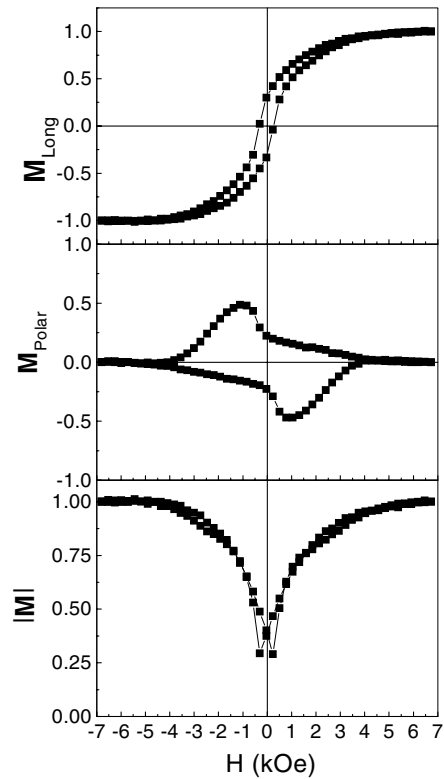
Figure 21. Magneto-optical vector magnetometry data for a Ni film 50 A thick, showing the longitudinal component M_{long}, the polar component M_{polar}, and the magnetization modulus versus the in-plane magnetic field. From [67].

5.3. In situ investigation of Fe/Cu(110)

As already pointed out in the introduction, important progress in the study of magnetic films as thin as a few monolayers has recently been achieved through *in situ* SMOKE and BLS operation within the vacuum chamber where the films are grown. This offers the opportunity of studying magnetic films without any possibility of effects induced by a protective non-magnetic capping layer. In spite of this clear advantage, it is worth noticing that, apart from the pioneering BLS measurements of Hillebrands *et al* [70] on Fe/W(110) and of Scheurer *et al* [71] on Fe/Cu(100), the only recent combined *in situ* BLS and SMOKE experiments reported in the literature (except those reviewed here) have been concerned with Fe/Ag(100) films and date back to a few years ago [72]. This lack of data could be due to the fact that the BLS alignment and measurement procedure can be quite complex and time-consuming in the case of large UHV systems, located quite apart from the BLS apparatus. In order to make such procedure reliable and easy, we have set up a new UHV chamber at GHOST Laboratory, Perugia University, specially designed to be directly interfaced with the optical table for *in situ* BLS and SMOKE measurements and to allow the variation of both the incidence angle of the light and the in-plane angle of the applied magnetic field, with field intensity up to 6 kOe. As shown in figure 23, it is a compact chamber mounted on top of a mobile frame, equipped with standard UHV tools, such as electron-beam evaporators, a quartz micro-balance, LEED–Auger apparatus, and a load-lock system. A horizontal XYZ manipulator, with primary and
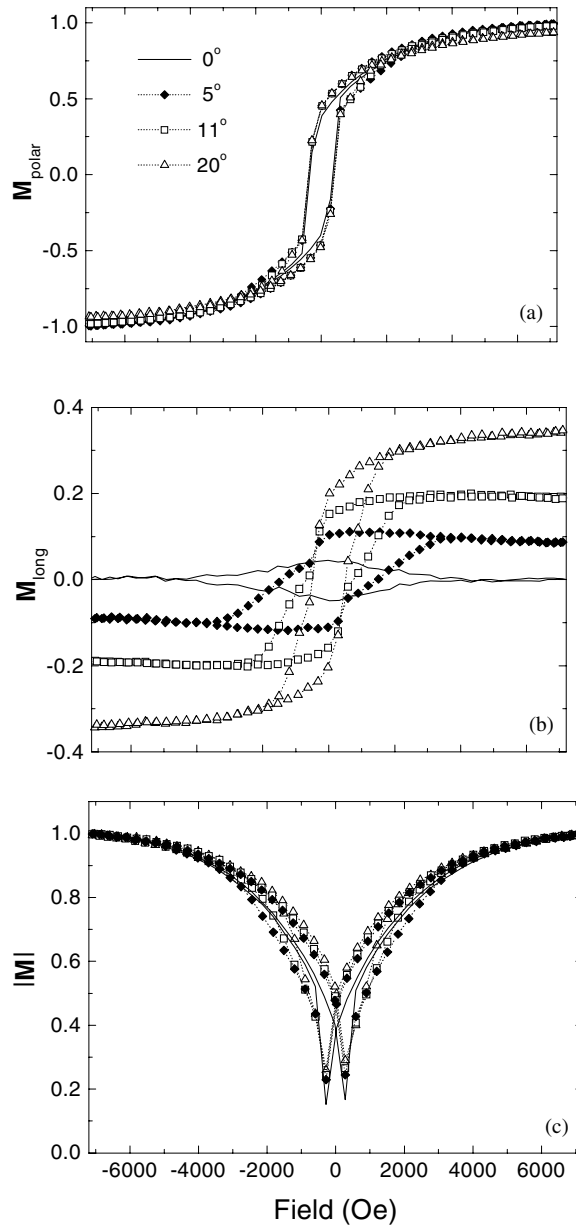
Figure 22. Magneto-optical vector magnetometry data in a canted-field geometry, showing the field dependence of: (a) the polar component of the magnetization, (b) the longitudinal component, (c) the magnetization modulus. All quantities are normalized to the saturation value. The field was applied at different angles with respect to the film normal. From [67].

secondary rotations, is used to position the evaporated film at the end of the so-called *BLS tube* which is a protuberance about 20 cm long and 10 cm in diameter, terminating with a glass viewport for BLS and SMOKE measurements. The temperature of the specimen can be varied in the range 110–1400 K. The whole frame can be translated, inserting the BLS tube within the poles of an external four-inch electromagnet, just beside the BLS optical table. The first results obtained using this apparatus have been published recently [73–75].
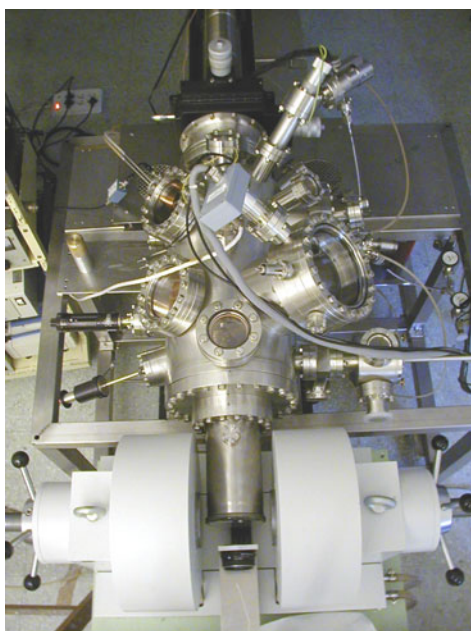
Figure 23. A top-view photograph of the UHV chamber used for *in situ* BLS and SMOKE measurements. From [74].

Fe films, with thickness in the range between 1 and 100 Å, were grown at room temperature on Cu(110) single crystal by electron-beam evaporation in UHV. LEED observations show clear p(1×1) patterns for deposited Fe layers up to a thickness of 4–6 Å with some diffuse background compared to the pattern observed for the Cu crystal. This is illustrated in figure 24. For higher coverages the diffuse background increases, and the LEED spots broaden and undergo a sort of splitting. This suggests that the first layers of Fe are epitaxial and that some disorder is gradually developing. Nevertheless, the LEED patterns keep the typical twofold symmetry induced by the fcc Cu(110) substrate up to the higher thicknesses investigated. A detailed structural characterization of the deposited Fe films has been done using x-ray reflectivity, x-ray diffraction, and photoemission diffraction at the Electra synchrotron radiation facility, beamline ALOISA [76]. The film structure is observed to be pseudomorphic with the substrate up to about 0.8 nm thickness. For larger thicknesses, Fe films undergo a structural transformation. Their in-plane lattice parameter closely resembles that of the bcc phase, while a 3D growth mechanism takes place, with islands elongated along the [001] direction of the substrate.

BLS measurements were performed *in situ* with the specimen put just behind the glass window at the end of the BLS tube. The external magnetic field, with a maximum intensity of 6 kOe, was applied parallel to the film plane and perpendicular to the scattering plane. Typical Brillouin spectra are shown in figure 25.

In figure 26 the values of the spin-wave frequencies of Fe films of different thicknesses are shown as a function of:

(a) the incidence angle of light θ for $H = 1.0$ kOe and $\phi_H = 0°$;
(b) the magnetic field intensity H ($\theta_i = 45°$ for $\phi_H = 0°$); and
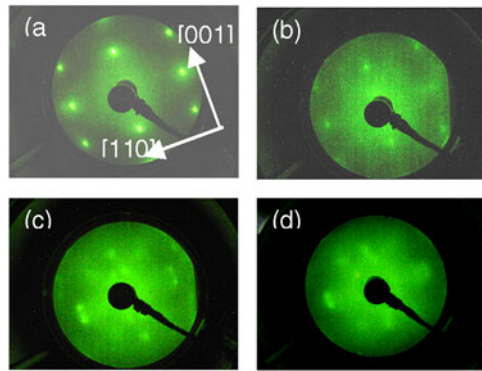(c) the in-plane direction of the magnetic field ϕ_H (for $H = 1.0$ kOe and $\theta_i = 20°$).

Figure 24. LEED patterns of (a) the Cu(110) single crystal, and Fe/Cu(110) films with nominal thicknesses of (b) 6 Å, (c) 40 Å, and (d) 100 Å. All LEED images were taken at 60 eV.
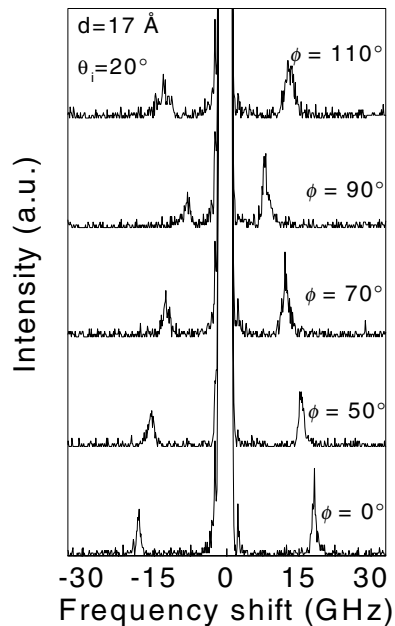

Figure 25. Brillouin spectra relating to the specimen that was 17 Å thick, measured for different values of the in-plane direction of the applied field. The intensity of the applied field is 1 kOe. From [74].

The data of figure 26(a) show that the spin-wave frequency dispersion increases with the thickness of the Fe films, as expected for the DE mode, while the almost linear dependence on the applied field (figure 26(b)) indicates that all of these Fe films are in-plane magnetized. In figure 26(c), the spin-wave frequencies display a twofold symmetry as a function of ϕ_H. The maxima of the spin-wave frequencies, indicating the easy-magnetization directions, are found at $\phi_H = 0$, clearly exhibiting an in-plane twofold symmetry induced in the Fe film by the Cu(110) substrate.
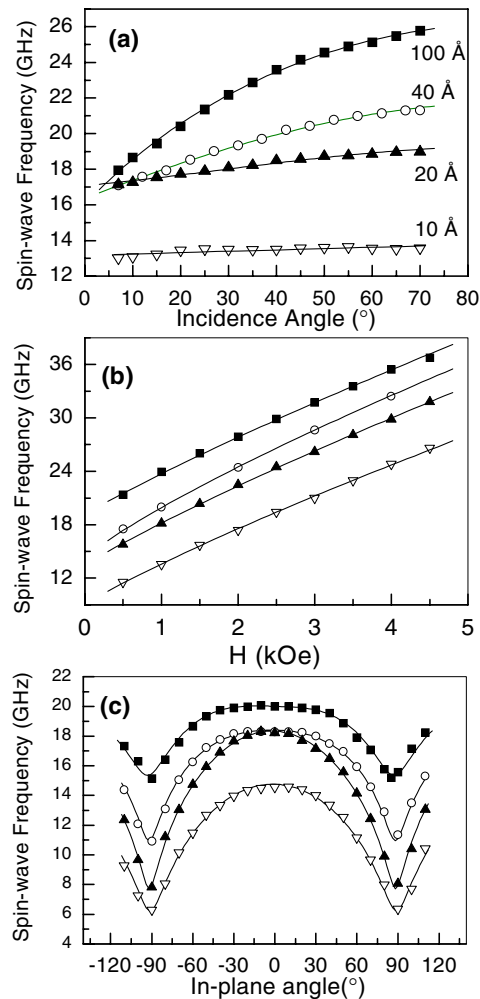
Figure 26. Experimental BLS spin-wave frequencies for different Fe films measured as a function of: (a) the incidence angle of light; (b) the field intensity H; and (c) the in-plane direction of the magnetic field (ϕ_H). Continuous curves are obtained by a simultaneous fitting of all the magnetic parameters using the equation reported in the text. From [73].

An even more detailed presentation of the effect of the strong uniaxial anisotropy, with magnetic 'easy' and 'hard' directions along the [001] and [1$\bar{1}$0] directions of the Cu substrate, respectively, is evidenced in figure 27 by the different shape of the hysteresis loops measured by the SMOKE technique, as well as by the characteristic non-monotonic dependence of the spin-wave frequency as a function of the external magnetic field applied along the hard direction. In particular, an external field of about 700–800 Oe is required to reach saturation of the hysteresis loop along the [1$\bar{1}$0] direction. This is reflected in the pronounced minimum in the evolution of the spin-wave frequency shown in figure 27. Remarkably, this uniaxial anisotropy, with the easy-magnetization axis along the [001] direction, persisted even in iron films as thick as 100 Å, where the LEED patterns indicated a disordered surface, at least on a long-range scale.
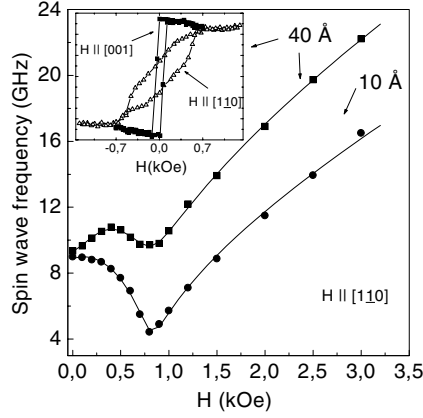
Figure 27. Spin-wave frequencies, measured by the BLS technique for two different Fe films, with thicknesses of 10 and 40 Å. The points show the measured values, while the lines are the best-fit curves. The external magnetic field H is applied along the magnetic hard axis (i.e. the $[1\bar{1}0]$ direction of the Cu substrate), while the angle of incidence of the light is kept fixed at 45°. In the upper inset, the hysteresis cycles corresponding to the above two directions are shown for the 4 nm thick specimen.

The magnetic parameters of the Fe films, together with their thicknesses, are determined by a simultaneous best-fitting procedure applied to the spin-wave frequencies as a function of θ, H, and ϕ_H, by using the analytical formula valid for an in-plane-magnetized thin film:

$$\left(\frac{\omega}{\gamma}\right)^2 = \left(H\cos(\phi_H - \phi) + \frac{2A}{M_s}q_\parallel^2 + \frac{1}{M_s}\left(2K_p^{(2)}\cos^2\phi - K_p^{(4)}\sin^2 2\phi - 2\frac{k_s}{d_{\text{Fe}}}\right)\right.$$
$$+ 4\pi M_s(1 - q_\parallel d_{\text{Fe}}/2)\Bigg)\Bigg(H\cos(\phi_H - \phi) + \frac{2A}{M_s}q_\parallel^2$$
$$+ \frac{2}{M_s}(K_p^{(2)}(1 - 2\sin^2\phi) + K_p^{(4)}(1 - 2\sin^2 2\phi)) + 2\pi M_s q_\parallel d_{\text{Fe}}\Bigg) \qquad (18)$$

with ϕ_H and ϕ measured from the in-plane reference axis [001]. This is a simplified version of equation (6), including $K_p^{(2)}$ and $K_p^{(4)}$ and k_s, which are the phenomenological in-plane uniaxial, in-plane fourfold, and out-of-plane interface anisotropy constants, respectively. Concerning the fitting results, which are summarized in [73, 74], we note that the film thicknesses are in fairly good agreement with the nominal ones, while the values of the saturation magnetization increase with the Fe film thickness, approaching the value of 21 kOe expected for bulk iron. As for the magnetic anisotropy, the dominant twofold symmetry persists even in the thickest film analysed and in order to reproduce the measured frequencies an appreciable fourfold in-plane anisotropy contribution must be included to improve the fit quality, although the values of $K_p^{(4)}$ obtained are much lower than those of the twofold anisotropy constant and are affected by rather large errors.

5.4. Effect of finite lateral dimension: submicrometric circular dots of permalloy

The last selected application of a combined BLS and MOKE study of magnetic systems is concerned with a rapidly emerging research field, i.e. that of magnetic patterned microstructures. To date, most of the BLS studies of patterned arrays of wires and dots has been carried out by the group of Hillebrands at Kaiserslautern University [77, 78] and by
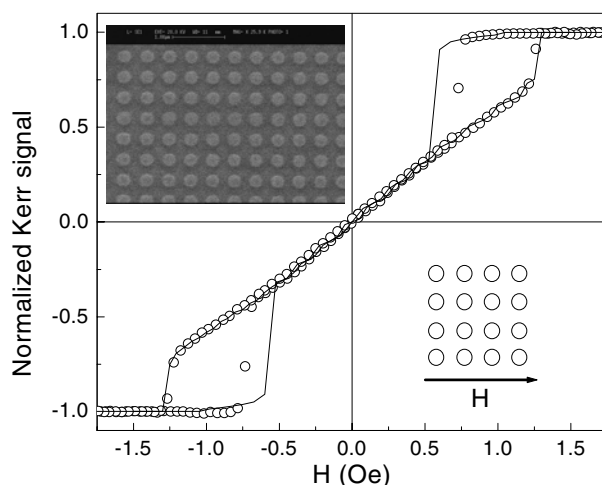
Figure 28. Measured (open circles) and simulated (continuous curve) hysteresis loops for the 0.2 μm diameter dots. The insets show the SEM image of the sample and the orientation of the applied field with respect to the dot arrays.

Grimsditch and co-workers at Argonne National Laboratory [79–81]. In particular, they have applied the BLS technique to measure the spin-wave dispersion on a regular square array of tangentially magnetized circular dots of permalloy. Although a detailed calculation of the spin-wave frequency is quite complicated because of the finite lateral shape of the dots, a theoretical model has been recently proposed by Guslienko and Slavin [82, 83] which enables one to calculate the spin-wave frequency in tangentially magnetized cylindrical dots, under the hypothesis of uniform magnetization. The frequency quantization is thus explained as a direct consequence of the boundary conditions at the lateral edges of the magnetic wires.

Here, recent results [84] on both the static and the dynamical magnetic properties of permalloy circular dots with a vortex domain configuration are reviewed. The dots have thicknesses of $L = 50$ nm and radii of $R = 0.1$ μm. A scanning electron microscopy image is shown in the inset of figure 28.

The magnetization configuration of the permalloy dots was investigated by measuring MOKE hysteresis loops with the external field applied parallel to the sample plane. A typical loop is shown in figure 28. In order to achieve an understanding of the MOKE loop in terms of the evolution of the magnetization configuration, the publicly available National Institute of Standards and Technology micromagnetic simulator [85], in which a numerical finite-element method is used to find the magnetization vector which solves the Landau–Lifshitz equation, was used. The integration is stopped when the torque reaches a value sufficiently low that the magnetization no longer evolves significantly (convergence parameter 10^{-5}). The crystalline anisotropy was set to zero since the measured in-plane anisotropy in our continuous layer was very small. Moreover, since the distance between the dots is the same as the diameter, the magnetic interaction among the dots may be considered negligibly small. The main features of the hysteresis loop are fairly well reproduced by the micromagnetic calculation (continuous curve in figure 28), where the magnetic parameters of permalloy derived from the BLS study of the continuous film were used (see below). At zero applied field the remanence is vanishing, a typical feature of a vortex remanent state of soft permalloy dots of circular shape. As the external field is switched on, the gradual increase of the magnetization corresponds to the moving of the vortex core from the centre to the outside. This is evident in the 2D vector
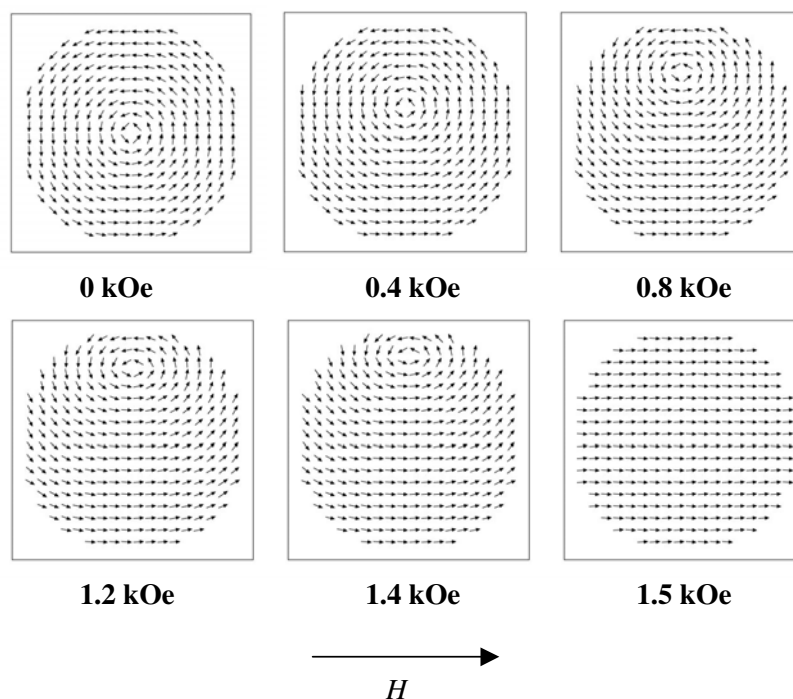
Figure 29. Magnetization configurations of each squared dot calculated by micromagnetic simulations, for different values of the applied magnetic field.

plots obtained from numerical micromagnetic calculations shown in figure 29. At zero field the vortex is in the centre and during the reversible part of the loop (at 0.6 and −0.6 kOe) the vortex core movement is perpendicular to the applied field and displaced toward the dot edges. On increasing the applied field the saturation is reached through a jump of magnetization at about 1.4 kOe. When the field is reduced from saturation, the cycle is non-reversible and a second jump takes place at about 0.7 kOe. The slight discrepancy between the measured and the simulated value of this second jump is typical of micromagnetic simulations and depends on the parameters of the model (cell size, convergence parameter, loop step). The existence of a vortex spin distribution was confirmed by magnetic force microscopy observation of magnetic domains [86].

As regards the dynamical magnetic properties, in figure 30 the BLS spectrum of the arrays of circular dots with radii $R = 0.1$ μm is shown together with the spectrum of the unpatterned permalloy film. The two spectra were taken under the same experimental conditions: incidence angle of light $\theta = 26°$ and magnetic field of 1.8 kOe to ensure sample saturation (as seen in the last simulation of figure 29). For the patterned film (upper spectrum), one notes the well resolved discretization of the peaks, indicated by the arrows, on both the Stokes and the anti-Stokes sides of the spectrum, while for the continuous films only one peak, associated with the DE, is present. The measured frequencies are (in GHz): 8.05, 9.30, 11.62, 14.65, and 16.02. Remarkably, it was found that the discrete modes are dispersionless, i.e. their frequencies do not change as a function of the magnon wavevector, and that their frequency increases monotonically with the intensity of the magnetic field.
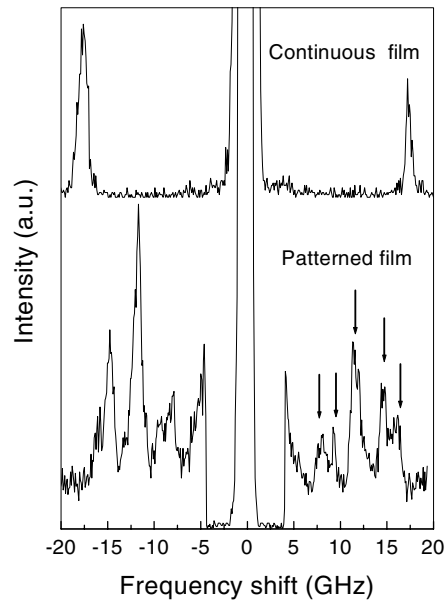
Figure 30. BLS spectra relating to the patterned film (lower spectrum) and the unpatterned film (upper spectrum). An in-plane external field of 1.8 kOe was applied while the incidence angle of light was $\theta = 26°$. Note that the two peaks close to the central elastic peak are artefacts produced by the closing of the mechanical shutter on the primary laser beam.

From a best-fit procedure applied to the frequency dependence of the DE mode of the continuous film on both the field intensity and the magnon wavevector, the values of the saturation magnetization $4\pi M_s = 8.8$ kOe, of the exchange stiffness constant $\alpha/4\pi = 1.93 \times 10^{-13}$ cm^2, and of the gyromagnetic ratio $\gamma = 2.95$ GHz kOe^{-1} were determined. These values have been used both in the micromagnetic simulation (solid curve in figure 25) and in the spin-wave frequency calculation. For the aspect ratio of our dots the effective demagnetizing factor (F), also entering into the frequency expression, can be calculated using an analytic formula which gives $F = -0.18$. In order to calculate the spin-wave frequency of the quantized modes of a cylindrical permalloy dot of radius $R = 0.1$ μm and height $L = 50$ nm the formalism recently proposed by Guslienko and Slavin [82, 83] has been exploited. The model is valid for an isolated cylindrical magnetic dot (i.e. $L/R \ll 1$) with in-plane magnetization in the presence of intradot dipolar and exchange interactions. The quantization condition on the parallel magnon wavevector has been introduced through the general boundary condition at the dot boundary $\rho = R$ in the absence of pinning on the cylindrical lateral surface. The five lowest mode frequencies have been calculated using the analytical equation for the frequency in the case of an external field $H = 1.8$ kOe. The diagonal frequencies calculated in the cosine basis corresponding to the Brillouin experimental geometry (in-plane wavevector perpendicular to saturation magnetization) are the following (in GHz): 9.51, 11.51, 12.73, 14.00, and 16.73. The lowest-frequency mode is the uniform mode of a single disc calculated with Kittel's formula [87]. These calculated frequencies compare fairly well with the experimental ones except for the two lowest modes, for which there is appreciable overestimation. The reason for this disagreement may be that for our dots the condition $L/R \ll 1$ is not rigorously fulfilled. In addition, the pinning at the lateral surface, neglected in the calculations, could reduce the theoretical frequency of the low-frequency modes.

6. Conclusions

In conclusion, the main characteristics of both the BLS and the SMOKE technique have been outlined and a number of applications to the study of magnetic nanostructures have been reviewed. We hope that the reader is now convinced that the simultaneous and combined use of these two techniques can yield relevant information concerning both the static and the dynamical magnetic properties of such systems. A natural development of both techniques will be the achievement of a lateral resolution well beyond the micrometric scale; this can be achieved by their integration in a scanning near-field optical microscope.

Acknowledgments

References

[1] Hillebrands B 2000 *Light Scattering in Solids* vol 7, ed M Cardona and G Guntherodt (Berlin: Springer) pp 174–269
[2] Carlotti G and Gubbiotti G 1999 *Riv. Nuovo Cimento* **22** 1
[3] Dutcher J R 1994 *Linear and Non-Linear Spin Waves in Magnetic Films and Superlattices* ed M G Cottam (Singapore: World Scientific) pp 287–333
[4] Demokritov S O and Tsymbal E 1994 *J. Phys.: Condens. Matter* **6** 7145
[5] Bader S D and Erskine J L 1994 *Ultrathin Magnetic Structures* vol 2, ed B Heinrich and J A C Bland (Berlin: Springer) pp 297–325
[6] Qiu Z Q and Bader S D 2000 *Rev. Sci. Instrum.* **71** 1243
[7] Phillips T G and Rosenberg H M 1966 *Rep. Prog. Phys.* **29** 285
[8] D'Orazio F, Lucari F, Carlotti G, Gubbiotti G, Carbucicchio M and Ruggiero G 2001 *J. Magn. Magn. Mater.* **226–30** 1767
[9] Hubert A and Schafer R 2000 *Magnetic Domains* (Berlin: Springer) pp 24–52
[10] Hubert A and Schafer R 2000 *Magnetic Domains* (Berlin: Springer) pp 86–7
[11] Mermin N D and Wagner H 1966 *Phys. Rev. Lett.* **17** 1133
[12] Pokroskii V L and Feigelmann M V 1977 *Sov. Phys.–JETP* **45** 291
[13] Wilhelm F, Bovensiepen U, Scherz A, Poulopoulos P, Ney A, Wende H, Ceballos G and Baberschke K 2000 *J. Magn. Magn. Mater.* **222** 163
[14] http://www.fisica.unipg.it/infm/ghost/ghost.HTM
[15] Jaquinot P 1960 *Rep. Prog. Phys.* **23** 268
[16] Sandercock J R 1982 *Light Scattering in Solids* vol 3, ed M Cardona and G Güntherodt (Berlin: Springer) p 173
[17] Nizzoli F and Sandercock J R 1990 *Dynamical Properties of Solids* vol 6, ed G K Horton and A A Maradudin (Amsterdam: North-Holland) p 307
[18] Vavassori P 2000 *Appl. Phys. Lett.* **77** 1605
[19] Vavasssori P *et al* 1999 *Phys. Rev.* B **59** 6337
[20] Cottam M G and Tilley D R 1999 *Introduction to Surface and Bulk Superlattice Excitations* (Cambridge: Cambridge University Press) p 183
[21] Néel L 1954 *J. Physique Radium* **15** 376
[22] Rado G T and Hicken R J 1988 *J. Appl. Phys.* **63** 3885
[23] Cochran J F and Dutcher J R 1988 *J. Appl. Phys.* **63** 3814
[24] Hillebrands B 1988 *Phys. Rev.* B **37** 9885
[25] Hillebrands B 1990 *Phys. Rev.* B **41** 530
[26] Stamps R L and Hillebrands B 1991 *Phys. Rev.* B **44** 5095
[27] Stamps R L and Hillebrands B 1991 *J. Appl. Phys.* **69** 5718
[28] Stamps R L and Hillebrands B 1991 *J. Magn. Magn. Mater.* **93** 616
[29] Gubbiotti G, Carlotti G and Hillebrands B 1998 *J. Phys.: Condens. Matter* **10** 2171

[30] Mills D L 1989 *Phys. Rev.* B **39** 12 306
[31] O'Handley R C and Woods J P 1990 *Phys. Rev.* B **42** 6568
[32] Chicazumi S 1964 *Physics of Magnetism* (New York: Wiley)
[33] Heinrich B, Celinski Z, Cochran J F Arrott A S and Myrtle K 1990 *Phys. Rev.* B **44** 530
[34] Damon R W and Eshbach J R 1961 *J. Phys. Chem. Solids* **19** 308
[35] Stamps R L and Hillebrands B 1991 *Phys. Rev.* B **43** 3532
[36] Ha K and O'Handley R C 2000 *J. Appl. Phys.* **87** 5944
[37] Rado G T and Weertmann J R 1959 *J. Phys. Chem. Solids* **11** 315
[38] Grimsditch M, Kumar S and Fullerton E 1996 *Phys. Rev.* B **54** 3385
[39] Vavassori P, Grimsditch M and Fullerton E 2001 *J. Magn. Magn. Mater.* **223** 284
[40] Fullerton E E, Jiang J S, Grimsditch M, Sowers C H and Bader S D 1998 *Phys. Rev.* B **58** 12 193
[41] Jiang S, Fullerton E, Grimsditch M, Sowers C H, Pearson J and Bader S 2000 *Phil. Mag.* B **80** 247
[42] Gubbiotti G, Albini L, Tacchi S, Carlotti G, Gunnella R and De Crescenzi M 1999 *Phys. Rev.* B **60** 17 150
[43] De Crescenzi M, Gunnella R, Bernardini R, De Marco M and Davoli I 1995 *Phys. Rev.* B **52** 1806
[44] Gubbiotti G, Albini L, Carlotti G, Socino G, Fusari S and De Crescenzi M 1999 *Surf. Sci.* **433–5** 685
[45] Gubbiotti G, Carlotti G, Socino G, D'Orazio F, Lucari F, Bernardini R and De Crescenzi M 1997 *Phys. Rev.* B
        56 11 073
[46] Gubbiotti G, Albini L, Carlotti G, Socino G, De Crescenzi M, Loreti S and Minarini C 1999 *Surf. Sci.* **433–5**
        680
[47] Zangwill A 1988 *Physics of Surfaces* (Cambridge: Cambridge University Press) p 422
[48] Ramirez R, Rahman A and Schuller I K 1984 *Phys. Rev.* B **30** 6208
[49] Kobayashi A and Das Sarma S 1987 *Phys. Rev.* B **35** 8042
[50] Bauer E and van der Merwe J H 1986 *Phys. Rev.* B **33** 3657
[51] Gubbiotti G, Carlotti G, D'Orazio F, Lucari F, Gunnella R and De Crescenzi M 2000 *Surf. Sci.* **449** 218
[52] Shen J, Klaua M, Ohresser P, Jenniches H, Barthel J, Mohan Ch V and Kirschner J 1997 *Phys. Rev.* B **56**
        11 134
[53] Zak J, Moog E R, Liu C and Bader S D 1990 *J. Magn. Magn. Mater.* **89** 107
[54] Gradmann U, Kummerle W and Williams P 1976 *Thin Solid Films* **34** 249
[55] Qiu Z Q, Pearson J and Bader S D 1992 *Phys. Rev.* B **45** 7211
[56] Paoluzi A 1988 *Magnetic Properties of Matter* ed F Borsa and V Tognetti (Singapore: World Scientific) p 56
[57] Pechan M J and Schuller I K 1987 *Phys. Rev. Lett.* **59** 132
[58] Pechan M J, Fullerton E E, Robertson W and Grimsditch M 1995 *Phys. Rev.* B **52** 3045
[59] Wohlfarth E P 1980 *Ferromagnetic Materials* ed E P Wohlfarth (Amsterdam: North-Holland) p 39
[60] Camley R E, Grünberg P and Mayr C M 1982 *Phys. Rev.* B **26** 2609
[61] Grünberg P 1989 *Light Scattering in Solids (Springer Topics in Applied Physics vol 5)* ed M Cardona and
        G Güntherodt (Berlin: Springer) and references therein
[62] Heinrich B, Celinski Z, Cochran J F, Arrott A S and Myrtle K 1991 *J. Appl. Phys.* **70** 5769
[63] Jungblut R, Johnson M T, aan de Stegge J, Reinders A and den Broeder F J A 1994 *J. Appl. Phys.* **75** 6424
        Huang F, Kief M T, Mankey G J and Willis R F 1994 *Phys. Rev.* B **49** 3962
        Schulz B and Baberschke K 1994 *Phys. Rev.* B **50** 13 467
        Farle M, Mirwald-Shulz B, Anisimov A N, Platow W and Baberschke K 1997 *Phys. Rev.* B **55** 3708
[64] Bochi G, Ballentine C A, Inglefield H E, Thompson C V, O'Handley R C, Hug H J, Stiefel B, Moser A and
        Guntherodt H-J 1995 *Phys. Rev.* B **52** 7311
[65] Gubbiotti G, Albini L, Carlotti G, Pini M G, Politi P, Rettori A, Ha K, Ciria M and O'Handley R C 2001 *J. Appl.
        Phys.* **89** 7386
[66] Gubbiotti G, Carlotti G, Ciria M and O'Handley R C 2002 *IEEE Trans. Magn.* submitted
[67] Gubbiotti G, Carlotti G, Pini M G, Politi P, Rettori A, Vavassori P, Ciria M and O'Handley R C 2002 *Phys. Rev.*
        B at press
[68] Murayama A, Hyomi K, Eickmann J and Falco C M 1988 *Phys. Rev.* B **58** 8596
        Murayama A, Hyomi K, Eickmann J and Falco C M 2000 *Phys. Rev.* B **61** 8984
[69] Ha K and O'Handley R C 1999 *J. Appl. Phys.* **85** 5282
[70] Hillebrands B, Baumgart P and Guntherodt G 1988 *Phys. Rev.* B **36** 2450
        Baumgart P, Hillebrands B and Guntherodt G 1991 *J. Magn. Magn. Mater.* **93** 225
[71] Scheurer S, Allenspach R, Xhonneux P and Courtens E 1993 *Phys. Rev.* B **48** 9890
[72] Hicken R J, Ercole A, Gray S J, Daboo C and Bland J A C 1996 *Appl. Phys.* **79** 4987
        Hicken R J, Gray S J, Ercole A, Daboo C, Freeland D J, Gu E, Ahamad E and Bland J A C 1997 *Phys. Rev.* B
        55 5898
[73] Gubbiotti G, Carlotti G, Madami M, Tacchi S and Verdini L 2002 *Phys. Status Solidi* a **189** 403

[74] Albini L, Carlotti G, Gubbiotti G, Madami M and Tacchi S 2001 *J. Appl. Phys.* **89** 7383
[75] Tacchi S, Albini L, Gubbiotti G, Madami M and Carlotti G 2002 *Surf. Sci.* **507–510C** 324
[76] Tacchi S, Bruno F, Carlotti G, Cvetko D, Floreano L, Gubbiotti G, Madami M, Morgante A, Verdini A 2002 *Surf. Sci.* **507–510C** 324
[77] Demokritov S and Hillebrands B 2002 Spin waves in laterally confined magnetic structures *Spin Dynamics in Confined Magnetic Structures* ed B Hillebrands and K Ounadjela (Berlin: Springer) pp 65–92 and references therein
[78] Jorzick J, Demokritov S O, Hillebrands B, Bartenlian B, Chappert C, Decanini D, Rousseaux F and Cambril E 1999 *Appl. Phys. Lett.* **75** 3859
[79] Grimsditch, Jaccard Y and Schuller I K 1998 *Phys. Rev.* B **58** 11 539
[80] Guedes I, Metlushko V, Zaluzec N, Grimsditch M, Vavassori P, Ilic B, Neuzil P and Kumar R 2000 *Phys. Rev.* B **62** 11 719
[81] Grimsditch M, Guedes I, Vavassori P, Metlushko V, Ilic B, Neuzil P and Kumar R 2001 *J. Appl. Phys.* **89** 7096
[82] Guslienko K Yu and Slavin A N 2000 *J. Magn. Magn. Mater.* **215** 576
[83] Guslienko K Yu and Slavin A N 2000 *J. Appl. Phys.* **87** 6337
[84] Gubbiotti G, Carlotti G, Zivieri R, Nizzoli F, Okuno T and Shinjo T 2002 *IEEE Trans. Magn.* at press
[85] http://math.nist.gov/oommf
[86] Shinjo T, Okuno T, Hassdorf R, Shigeto K and Ono T 2000 *Science* **289** 930
[87] Kittel C 1948 *Phys. Rev.* **73** 155